



Chapter 5: Fourier Transform Spectroscopy

The idea of ~~using~~ Fourier transform spectroscopy was born from a very different natured project. The project was originally conceived as a way to engineer tunable spin-orbit coupling using multiple-tone Raman transitions. The inspiration came from a previous project where we used multiple-tone Raman transitions to engineer a spin-1 spin-orbit coupled system whose ground state presented different magnetic phases [4]. Fourier spectroscopy was conceived as a new way to characterize the tunable dispersion relation resulting from our proposed coupling scheme. Unfortunately, we realized that this proposal was equivalent to another experiment that achieved tunable SOC using amplitude modulated Raman coupling [5]. We therefore decided to focus on studying Fourier spectroscopy instead, a decision that turned out to be very fruitful for our lab as we continue to use this technique to characterize the spectrum of a variety of systems ~~to this date~~.

Many spectroscopy techniques in atomic physics rely on using a source of coherent electromagnetic radiation with a well known frequency that probes the internal structure of a system (atom). For example, in absorption spectroscopy [6] ~~a~~ coherent light ~~source~~ is sent through an atomic medium and if the frequency of the light is resonant with an atomic transition it will be absorbed and a reduced transmission will be measured. Other variants of spectroscopy (e.g. Rabi spectroscopy [7], spin-injection spectroscopy [8]) work under a similar principle: atoms absorb and emit photons with frequencies equal to the transition energies between internal states.

Fourier transform spectroscopy instead employs the connection between the energy spectrum of a system and its dynamics. This connection has been exploited to study the spectrum of both condensed matter [9] and cold atom systems [10, 11] alike. As opposed to other techniques, Fourier spectroscopy relies only on following the unitary evolution of an initial state suddenly subjected to a Hamiltonian of interest and measuring probabilities in a basis that does not diagonalize that Hamiltonian.

The frequency resolution of Fourier transform spectroscopy is limited only by the coherent evolution timescale of the system under study and can otherwise be applied to any system. Other applications of this technique implemented in our lab that are not included in this Chapter include measuring the dispersion relation of a Rashba spin-orbit coupled gas (see Chapter 8) and the band structure of a sub-wavelength optical lattice [12].

In this Chapter I will first give a general description of the Fourier transform spectroscopy technique in Section 5.1. Then in Section 5.2 I will describe a set of experiments where we engineered a tunable spin-orbit coupled system (our original goal) and applied Fourier transform spectroscopy . This work was published in [13].

5.1 Operating principle of Fourier spectroscopy

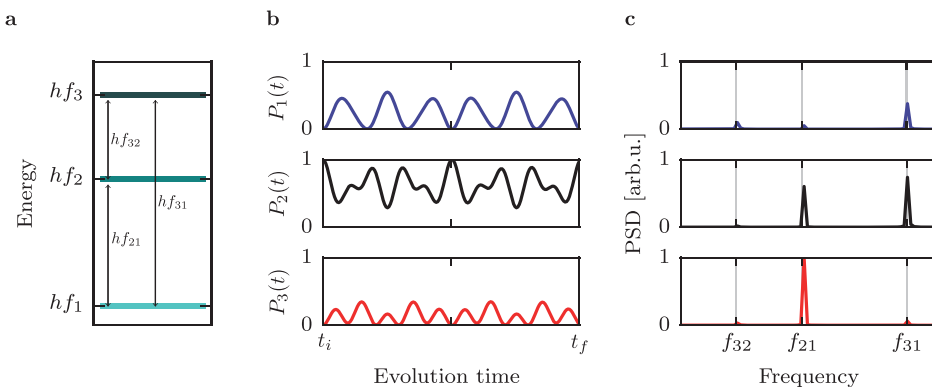


Figure 5.1: **a.** Eigenenergies of a three-level system described by $\hat{H}'(\Omega_1, \Omega_2, \Omega_3)$. **b.** The system is prepared in $|\psi_2\rangle$ and subjected to \hat{H}' at time t_i . The three panels show the occupation probabilities of the states $|\psi_1\rangle$ (blue), $|\psi_2\rangle$ (black), and $|\psi_3\rangle$ (red) in the measurement basis, for evolution times up to t_f . **c.** Power spectral density of the occupation probabilities from panel b. The three peaks in the Fourier spectra correspond to the energy differences present in panel a.

We focus on a system where we can measure the occupation probabilities of a set of orthonormal states $\{|\psi_i\rangle\}$ that fully span the accessible Hilbert space of the system. We then consider the time evolution of an arbitrary

initial state $|\Psi_0\rangle = \sum_i a_i |\psi_i\rangle$ as governed by a Hamiltonian $\hat{H}'(\{\Omega_i\})$ and observe the occupation probabilities of the $\{|\psi_i\rangle\}$ states of the measurement basis as a function of time. When \hat{H}' is applied, the evolution of the initial state is $|\Psi(t)\rangle = \sum_{i,j} a_i c_{i,j} e^{-iE'_j t/\hbar} |\psi'_j\rangle$, where E'_j and $|\psi'_j\rangle$ are the eigenenergies and eigenstates of \hat{H}' , and $c_{i,j}(t) = \langle \psi_i | \psi'_j \rangle$. The probability

$$P_k(t) = |\langle \psi_k | \Psi(t) \rangle|^2 = \left| \sum_{i,j} a_i c_{i,j} c_{j,k}^* e^{-iE'_j t/\hbar} \right|^2 \quad (5.1)$$

of finding the system in a state $|\psi_k\rangle$ of the measurement basis can be expressed as a sum of oscillatory components, with amplitude given by the magnitude of the overlap integrals between the initial state and the eigenvalues of \hat{H}'

$$P_k(t) = 1 + \sum_{i,j \neq l} 2|a_i^2 c_{i,j} c_{j,k} c_{l,k}| \cos(2\pi f_{j,l} t), \quad (5.2)$$

where $f_{j,l} = (E'_j - E'_l)/\hbar$ is the frequency associated with the energy difference of two eigenstates of the Hamiltonian. Fourier spectroscopy relies on measuring the populations on each state of the measurement basis as a function of time, and extracting the different frequency components $f_{j,l}$ directly by computing the discrete Fourier transform. The bandwidth and frequency resolution of the measurement are determined by the total sampling time and the number of samples. For N samples separated by a time interval Δt , the highest resolved frequency will be $f_{\text{bw}} = 1/2\Delta t$, with resolution $\Delta f = 1/\Delta t N$. This resolution can be decreased if the Fourier transform is calculated using certain types of windowing functions that enhance signal to noise. Any higher frequency $f > f_{\text{bw}}$ will be aliased and measured in the Fourier spectrum as $f_{\text{alias}} = |f - m/\Delta t|$, where m is an integer. If interactions are present in the system, the dynamics get modified in a time scale given by the magnitude of the interactions, giving an additional constraint to the smallest frequency components of a single particle Hamiltonian that can be resolved with our technique.

Figure 5.1 illustrates the principle of Fourier spectroscopy for a three level system, initially prepared in the state $|\Psi_0\rangle = |\psi_2\rangle$, subject to the Hamiltonian

$$\hat{H}' = \begin{pmatrix} E_1 & 0 & 0 \\ 0 & E_2 & 0 \\ 0 & 0 & E_3 \end{pmatrix} + \hbar \begin{pmatrix} 0 & \Omega_1 & \Omega_2 \\ \Omega_1^* & 0 & \Omega_3 \\ \Omega_2^* & \Omega_3^* & 0 \end{pmatrix}, \quad (5.3)$$

where we measure the occupation probability as a function of time for each of the $\{|\psi_1\rangle, |\psi_2\rangle, |\psi_3\rangle\}$ states. The three eigenenergies $E'_i = \hbar f_i$ that result from diagonalizing \hat{H}' are displayed in figure 5.1a. The three energy differences $\hbar f_{jj'}$ between the levels determine the oscillation frequencies of the occupation probabilities, as can be seen in figure 5.1b. Finally, a plot of the power spectral densities (PSD) in figure 5.1c shows three peaks at frequencies corresponding to the three relative energies of \hat{H}' .

5.2 Measuring the SOC dispersion with Fourier transform spectroscopy

5.2.1 System

We applied the Fourier transform spectroscopy technique to measure the dispersion relation of BECs with (tunable) SOC. All of our experiments started with BECs containing about 4×10^4 atoms in the $|f = 1, m_f = -1\rangle$ hyperfine state. The experiments described in Section 5.2.3 were performed in an optical dipole trap with frequencies $(\omega_x, \omega_y, \omega_z)/2\pi = (42(3), 34(2), 133(3))$ Hz. We later modified the trapping frequencies in the xy plane to try to make them more symmetric for the experiments described in Section 5.2.4. We broke the degeneracy of the three m_F magnetic sub-levels by applying a 1.9893(3) mT bias field along \mathbf{e}_z that produced a $\omega_Z/2\pi = 14.000(2)$ MHz Zeeman splitting, and a quadratic Zeeman shift ϵ that shifted the energy of $|f = 1, m_F = 0\rangle$ by $-\hbar \times 28.45$ kHz. We transferred atoms into the $|f = 1, m_F = 0\rangle$ state using ARP and then we monitored and stabilized the magnetic field using partial transfer absorption imaging as described in Chapter 4.5.2 by applying a pair of $250 \mu\text{s}$ microwave pulses, each of them detuned by ± 2 kHz from the $|f = 1, m_F = 0\rangle \leftrightarrow |f = 2, m_F = 1\rangle$ transition.

We induced spin-orbit coupling using a pair of intersecting, cross polarized Raman laser beams propagating along $\mathbf{e}_x + \mathbf{e}_y$ and $\mathbf{e}_x - \mathbf{e}_y$, as shown in figure 5.2a and b. These beams have angular frequency $\omega_A = \omega_L + \delta$ and $\omega_B = \omega_L + \omega_Z$, where 2δ is the, experimentally controllable, detuning from four photon resonance between $m_F = -1$ and $m_F = +1$.

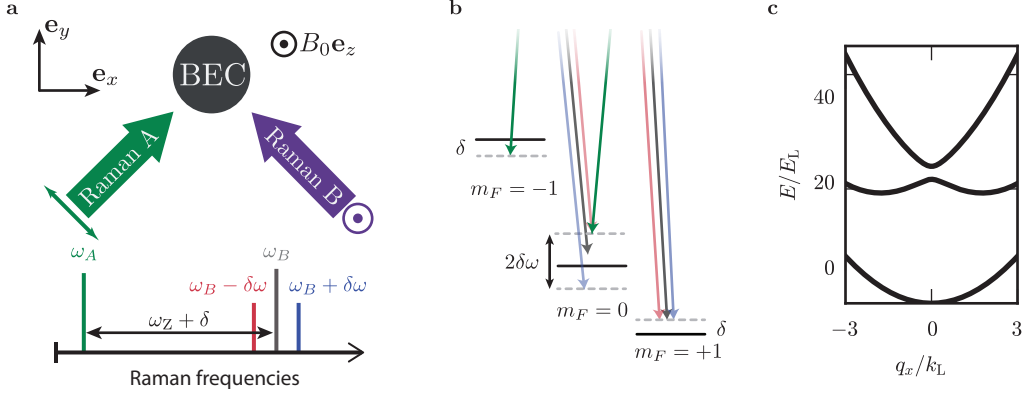


Figure 5.2: **a.** Setup. A bias magnetic field $B_0 \mathbf{e}_z$, with $B_0 = 1.9893$ mT splits the hyperfine energy levels of the $f = 1$ manifold of ^{87}Rb by $\omega_Z/2\pi = 14$ MHz. A pair of cross polarized Raman beams propagating along $\mathbf{e}_x + \mathbf{e}_y$ and $\mathbf{e}_x - \mathbf{e}_y$ couple the atoms' momentum and spin states. **b.** The Raman frequencies are set to $\omega_A = \omega_L + \delta$ and $\omega_B = \omega_L + \omega_Z$. We add frequency sidebands to ω_B , separated by $\pm\delta\omega$. The amplitude modulation from the interference between the multiple frequency components results in tunable SOC. **c.** SOC dispersion for Raman coupling strength $\Omega_0 = 12E_L$ and $\Omega = 0$, on four photon resonance.

Our system was well described by the Hamiltonian including atom-light interaction along with the kinetic contribution

$$\hat{H}_{\text{SOC}} = \frac{\hbar^2 q_x^2}{2m} + \alpha q_x \hat{F}_z + 4E_L \hat{\mathbb{1}} + \hbar\Omega_R \hat{F}_x + (4E_L - \epsilon)(\hat{F}_z^2 - \hat{\mathbb{1}}) + \hbar\delta\hat{F}_z, \quad (5.4)$$

where q is the quasimomentum, $\hat{F}_{x,y,z}$ are the spin-1 angular momentum matrices, $\alpha = \hbar^2 k_L/m$ is the SOC strength, and Ω_R is the Raman coupling strength, proportional to the Raman laser intensity. The Raman field coupled $|m_F = 0, q = q_x\rangle$ to $|m_F = \pm 1, q = q_x \mp 2k_L\rangle$, generating a spin change of $\Delta m_F = \pm 1$ and imparting a $\mp 2k_L$ momentum. The eigenstates of \hat{H}_{SOC} are linear combinations of these states and $|m_F = 0, q = q_x\rangle$, and the set $\{|m_F, q\rangle\}$ constituted the measurement basis for Fourier transform spec-

troscopy.

Figure 5.2c shows a typical band structure of our spin-1 SOC system as a function of quasimomentum for a large and negative quadratic Zeeman shift $-\epsilon > 4E_L$. In this parameter regime the ground state band has a nearly harmonic dispersion with an effective mass $m^* = \hbar^2[d^2E(k_x)/d^2x]^{-1}$, only slightly different from that of a free atom.

5.2.2 Tunable SOC

We engineered a highly tunable dispersion relation in which we can independently control the size of the gap at $q_x = 0$ as well as the SOC strength α by adding frequency sidebands to one of the Raman beams. The state of the system can change from $|m_F = -1, q = q_x + 2k_L\rangle$ to $|m_F = 1, q = q_x - 2k_L\rangle$ by absorbing a red detuned photon first followed by a blue detuned photon and vice versa, in a similar way to the Mølmer-Sørensen entangling gate in trapped ion systems [14]. When we set the angular frequencies of the sidebands to $\omega = \omega_A + \omega_Z \pm \delta\omega$, the Hamiltonian (Equation 5.4) acquired a time-dependent coupling $\Omega_R(t) = \Omega_0 + \Omega \cos(\delta\omega t)$. This periodically driven system is well described by Floquet theory [15] (see Chapter 4.6). Figure 5.3 shows the spectrum of Floquet quasi-energies for a system described by 5.4 where Ω_R oscillates with angular frequency $\delta\omega$.

We defined an effective, time-independent Hamiltonian \hat{H}_{Fl} that described the evolution of the system sampled stroboscopically at an integer number of driving periods, with the time evolution operator $\hat{U}(t_0, t_0 + T) = e^{-iT\hat{H}_{Fl}}$. One way of finding \hat{H}_{Fl} is to choose a clever unitary transformation $\hat{U}(t)$ such that the dynamics of the transformed wave function are described by a time independent Hamiltonian. Recall that the time evolution of a wave function in a transformed frame $|\psi'\rangle = \hat{U}^\dagger |\psi\rangle$ is given by the time dependent Schrödinger equation with a Hamiltonian $\hat{H}' = \hat{U}^\dagger \hat{H} \hat{U} - i\hbar \hat{U}^\dagger \partial_t \hat{U}$. Here we used

$$\hat{U}(t) = \exp[-i\frac{\Omega}{\delta\omega} \sin(\delta\omega t) \hat{F}_x] \quad (5.5)$$

so that $i\hbar \hat{U}^\dagger \partial_t \hat{U} = \hbar \Omega_R(t) \hat{F}_x$. The transformed Hamiltonian $\hat{H}'(t)$ has terms proportional to $\sin(\Omega/\delta\omega \sin(\delta\omega t))$, $\sin^2(\Omega/\delta\omega \sin(\delta\omega t))$, $\cos(\Omega/\delta\omega \sin(\delta\omega t))$ and $\cos^2(\Omega/\delta\omega \sin(\delta\omega t))$ which we simplified using the Jacobi-Anger expansion

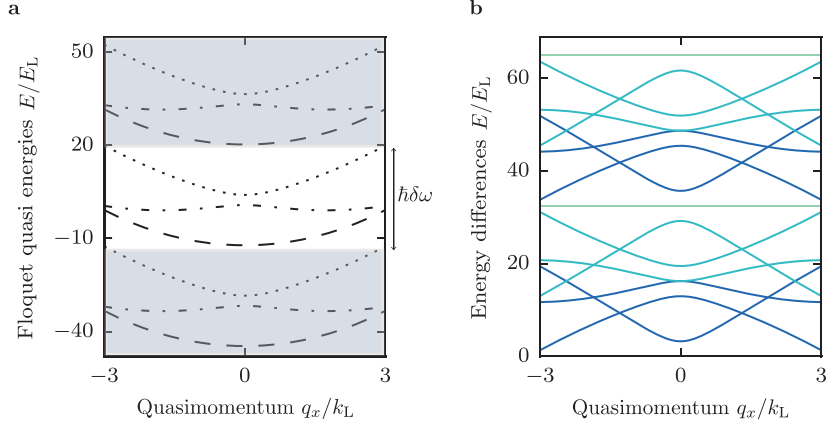


Figure 5.3: **a.** Floquet quasi-energies of a three level Hamiltonian with SOC and time periodic coupling strength. The quasi-energies are grouped into manifolds consisting of three levels that get repeated with a periodicity equal to $\hbar\delta\omega$. **b.** Energy differences of the Floquet quasi-energies. Each color represents the energy difference, separated by a fixed number of neighboring levels. When the number of neighboring levels is a multiple of 3, the energy differences are straight lines, a result of the periodic structure of the Floquet manifolds.

sion for large values of θ

$$\cos(z \sin \theta) = J_0(z) + 2 \sum_{n=1}^{\infty} J_{2n}(z) \cos(2n\theta) \approx J_0(z)$$

$$\sin(z \sin \theta) = 2 \sum_{n=0}^{\infty} J_{2n+1}(z) \sin((2n+1)\theta) \approx 0,$$

where J_n is the the n th order Bessel function of the first kind.

This approximation is valid for $\hbar\delta\omega > |\epsilon| + 12E_L$ and $|q_x| \leq 2k_L$ so that quasi-energy manifolds are well separated as in figure 5.3a. The Floquet Hamiltonian retained the form of Equation 5.4 with renormalized coefficients and an additional coupling term:

$$\hat{H}_{Fl} = \hat{H}_{SOC}(q, \Omega_0, \tilde{\alpha}, \tilde{\delta}, \tilde{\epsilon}) + \tilde{\Omega} \hat{F}_{xz}, \quad (5.6)$$

where $\tilde{\alpha} = J_0(\Omega/\delta\omega)\alpha$, $\tilde{\Omega} = 1/4(\epsilon + 4E_L)[J_0(2\Omega/\delta\omega) - 1]$, $\tilde{\delta} = J_0(\Omega/\delta\omega)\delta$, and $\tilde{\epsilon} = 1/4(4E_L - \epsilon) - 1/4(4E_L + 3\epsilon)J_0(2\Omega/\delta\omega)$. \hat{F}_{xz} is the λ_4 Gell-Mann matrix that directly couples $|m_f = -1, q = q_x + 2k_L\rangle$ and $|m_f = +1, q = q_x - 2k_L\rangle$ states. The experimentally tunable parameters $\delta\omega$, Ω and Ω_0 can be used to tune the SOC dispersion.

5.2.3 Application of Fourier spectroscopy

We used Fourier transform spectroscopy to measure the spectrum of the SOC Hamiltonian (Equation 5.6) for three coupling regimes: (i) $\Omega_0 \neq 0$ and $\Omega = 0$, (ii) $\Omega_0 = 0$ and $\Omega \neq 0$ and (iii) $\Omega_0 \neq 0$ and $\Omega \neq 0$. We turned on the Raman laser non-adiabatically, in approximately $1\mu\text{s}$. We let the system evolve subject to \hat{H}_{SOC} for up to $900\mu\text{s}$, and then turned off the laser while releasing the atoms from the optical dipole trap. As usual, we resolved the spin and momentum distribution using Stern-Gerlach and a 21 ms TOF which allowed us to measure the fraction of atoms in each state of the measurement basis $\{|m_F, q\rangle\}$. The density of sampling points and the maximum evolution time were chosen so that the bandwidth of the Fourier transform was comparable to, or larger than, the highest frequency in the evolution of the system while maximizing resolution. Experimental decoherence resulting in loss of contrast of the oscillations, which arises from magnetic field noise and small magnetic field gradients present in our apparatus, was an additional constraint that becomes significant around 1 ms.

In order to map the full spin and momentum dependent band structure of \hat{H}_{SOC} , we measured the time dependent occupation probabilities at a fixed Raman coupling strength and different values of Raman detuning δ , for the same initial state $|m_F = 0, q_x = 0\rangle$. This detuning corresponded to the Doppler shift experienced by atoms moving relative to a light source with quasimomentum $q_x/k_L = \hbar\delta/4E_L$. We controlled the frequency and the detuning of the Raman beams using two AOMs, one of which is driven by up to three phase coherent frequencies (the carrier frequency plus two sidebands). For each of the three coupling cases that we measured, we applied the Raman beams at detuning values within the interval $\pm 12E_L$ which corresponds to quasimomentum values $\pm 3k_L$.

This approach of changing detuning rather than using atoms with non-zero quasimomentum had the advantage that the state preparation was very

reliable (making BECs at rest is easy¹!) and we got very good signal to noise ratios due to the relatively high densities of the BECs. The downside is that if one is interested in looking at a large range of quasimomentum values, it takes a long time to repeat each experiment for different detuning values. In future experiments where we used Fourier transform spectroscopy we sacrificed some signal to noise for speed and used the momentum distribution of non-condensed atoms to parallelize our measurements.

5.2.4 Effective mass

Fourier transform spectroscopy only gives access to the relative energies of a Hamiltonian. If we want to recover the absolute energies we need to have an additional energy reference. For this particular set of experiments we had a ground state with a nearly quadratic dispersion and we could measure its effective mass which allowed us to obtain such reference.

We measured the effective mass of the Raman dressed atoms by adiabatically preparing the BEC in the lowest eigenstate and inducing dipole oscillations. The effective mass of the dressed atoms is related to the bare mass m and the bare and dressed trapping frequencies ω and ω^* by the ratio $m^*/m = (\omega/\omega^*)^2$. We measured this ratio following [16]; we start in $|m_F = 0, k_x = 0\rangle$ state and adiabatically turn on the Raman laser in 10 ms while also ramping the detuning to $\delta \approx 0.5 E_L$, shifting the minima in the ground state energy away from zero quasi-momentum. We then suddenly bring the field back to resonance, exciting the BEC's dipole mode in the optical dipole trap. We measured the bare state frequency by using the Raman beams to initially induce motion but subsequently turn them off in 1 ms and let the BEC oscillate. For this set of measurements, we adjusted our optical dipole trap to give new trapping frequencies $(\omega_x, \omega_y, \omega_z)/2\pi = (35.6(4), 32.2(3), 133(3))$ Hz, nominally symmetric in the plane defined by \mathbf{e}_x and \mathbf{e}_y . The Raman beams were co-propagating with the optical dipole trap beams; therefore, the primary axes of the dipole trap frequencies are at a 45° angle with respect to the direction of \mathbf{k}_L .

The kinetic and potential terms in the Hamiltonian including the contribution of the Raman and optical dipole trap were

¹Well, nothing in the lab is really ‘easy’...

$$\begin{aligned}\hat{H}_\perp &= \frac{\hbar^2 q_x^2}{2m^*} + \frac{\hbar^2 q_y^2}{2m} + \frac{m}{2} [\omega_{x'}^2 x'^2 + \omega_{y'}^2 y'^2] \\ &= \frac{\hbar^2}{2m^*} k_x^2 + \frac{1}{2m} k_y^2 + \frac{m}{4} [(\omega_{x'}^2 + \omega_{y'}^2)(x^2 + y^2) + 2xy(\omega_{x'}^2 - \omega_{y'}^2)],\end{aligned}\quad (5.7)$$

where we have used $x' = (x+y)/\sqrt{2}$ and $y' = (x-y)/\sqrt{2}$ to rotate the dipole trap coordinates by 45° . For an axially symmetric trap with $\omega_{x'} = \omega_{y'}$, the frequency of oscillation along the Raman recoil direction is

$$\omega_x^2 = \frac{m}{2m^*} (\omega_{x'}^2 + \omega_{y'}^2). \quad (5.8)$$

Our trap had a small 3.4 Hz asymmetry and therefore there is some coupling of the motion along the axis perpendicular to \mathbf{k}_L which becomes more significant at larger values of effective mass. The sampling times for the measurements were small compared to the trap asymmetry and therefore we can locally approximate the motion of the atoms by simple harmonic function with a frequency along \mathbf{e}_x given by Equation 5.8.

Figure 5.4 shows the dipole oscillations along the \mathbf{e}_x and \mathbf{e}_y directions for the three different coupling regimes we explored, as well as the bare state motion. The resulting mass ratios for the three coupling regimes are $m/m^* =$ (i) 1.04(8), (ii) 0.71(7), and (iii) 0.62(4).

5.2.5 Measured dispersion

We mapped the band structure of SOC atoms for three different coupling regimes. Figure 5.5a shows representative traces of the measured occupation probabilities for short evolution times along with fits to the unitary evolution given by \hat{H}_{SOC} with δ , Ω_0 , and Ω as free parameters. The fit parameters agree well with independent microwave and Raman power calibrations. In the lower two panels, where the Raman coupling strength was periodically modulated, the occupation probabilities oscillate with more than three frequencies since the full description of the system was given by a Floquet quasi-energy spectrum. Figure 5.5b,c shows the occupation probabilities for the parameter regime (iii) for longer evolution times along with the PSD of the occupation probability of each spin state.

We used a non-uniform fast Fourier transform algorithm (NUFFT) on

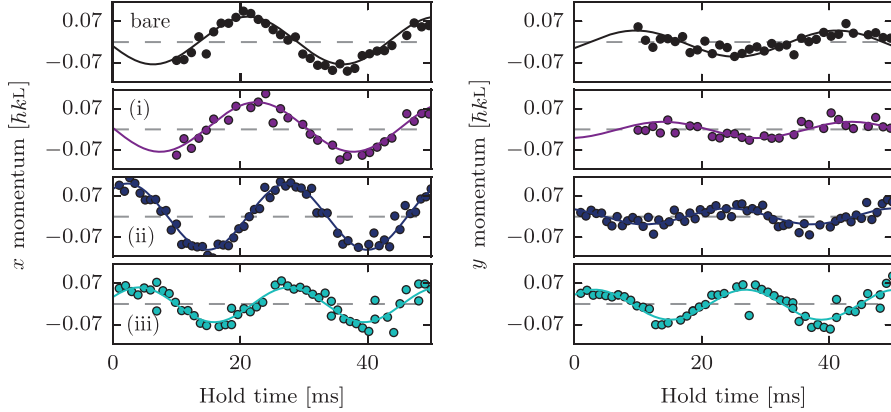


Figure 5.4: Oscillation of the BEC in the dipole trap along the recoil directions \mathbf{e}_x and \mathbf{e}_y for (top) bare atoms, and the three parameter regimes that we explored (i), (ii), and (iii). We believe that the observed low amplitude oscillations along \mathbf{e}_y are due to the initial detuning ramp not being fully adiabatic.

a square window to obtain the power spectral density of the occupation probabilities since our data points were not always evenly spaced because of imperfect imaging shots. The heights of the peaks in the PSD are related to the magnitude of the overlap integrals between the initial state and the Raman dressed states. Figure 5.5c shows the raw PSD of the time evolution of the system under \hat{H}_{SOC} for a given Raman coupling strength and detuning. We put together all the PSDs for the three coupling regimes in the spectra shown on the top three panels in figure 5.6. Each column corresponds to a different coupling regime and the colors represent the different spin states of the measurement basis. The spectra show that some overlap integrals vanish near $\delta = 0$, which is manifested as missing peaks in the PSD. The periodic structure of the Floquet quasi-energy spectrum gives rise to peaks at constant frequencies of $\delta\omega$ and $2\delta\omega$ independently of the Raman detuning, and a structure that is symmetric about the frequencies $2\pi f_1 = \delta\omega/2$ and $2\pi f_2 = \delta\omega$. If you are interested in seeing another nice experiment where the Floquet quasienergy spectrum becomes important due to breaking of the RWA see [17].

We obtained the characteristic dispersion of a SOC system after adding

a quadratic term to the PSD, proportional to the measured effective mass, and after rescaling the detuning into recoil momentum units. We combined the PSD of the time evolution of the three $|m_F\rangle$ states to look at the spin dependence of the spectra. Figure 5.7 shows the measured dispersion relations as well as the Floquet quasi-energies calculated for the Hamiltonian parameters obtained from our calibrations. The spectral lines that can be resolved with our technique depend on the overlap integrals of the initial state with the target Hamiltonian eigenstates. Additional energies can be measured by repeating the experiment with different initial states. The spectral lines we were able to resolve are in good agreement with the calculated energies of the Hamiltonian.

Finally, because it is not so trivial to visualize what we did to recover the dispersion for the periodically driven SOC cases, Figure 5.8 illustrates in detail the steps that were taken. The red line in panel a represents a level within a Floquet manifold that has the largest overlap integral with the initial $|m_F = 0, q = 0\rangle$ state. The peaks in the PSD correspond to energy differences between the marked level and the levels in neighboring Floquet manifolds pointed by the colored arrows. We show the theoretically computed energy differences on top of the measured PSD in panel b. The lowest frequency dominant peaks of the PSD correspond to energy differences with the adjacent lower Floquet manifold. To properly recover the SOC dispersion we ~~need to shift~~ the PSD by a negative quadratic term $-\hbar^2 q_x^2 / 2m^*$ as we show on panel c. We finally invert the frequency axis and shift it by $\delta\omega$. Including the effective mass to reconstruct the spectrum of the time-independent SOC case, amounts to shifting the PSD by a positive quadratic term.

Conclusion



We introduced the basic principles of the Fourier transform spectroscopy technique and used it to measure the spin and momentum dependent dispersion relation of a spin-1 spin-orbit coupled BEC. We additionally studied a periodically driven SOC system and found a rich Floquet quasi-energy spectrum. Our method can be applied generically to any system with long enough coherent evolution to resolve the energy scales of interest, and could prove particularly useful to study systems where it is harder to predict or compute the exact energies, such as cold atom realizations of disordered or highly correlated systems [18]. Moreover, this technique can be extended

with the use of spectrograms to study time dependent spectra, such as that of systems with quench-induced phase transitions.

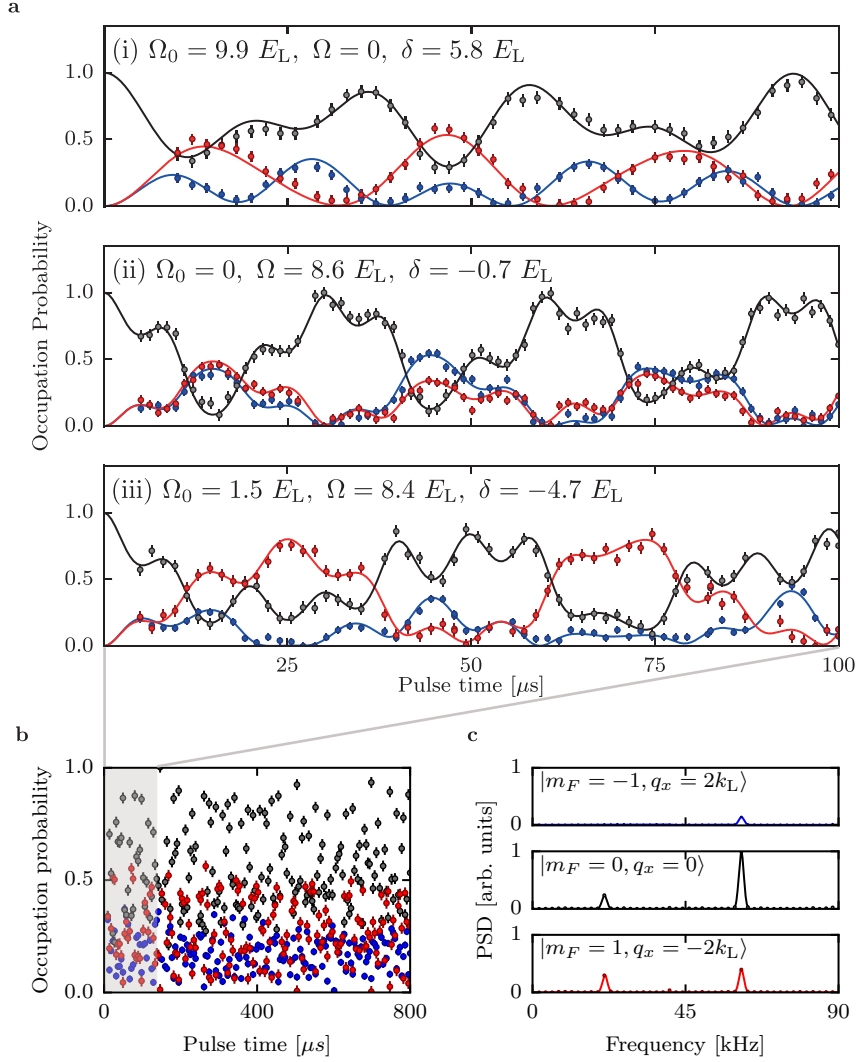


Figure 5.5: **a.** Occupation probability for the three states in the measurement basis $|m_f = -1, q = q_x + 2k_L\rangle$ (blue), $|m_f = 0, q = q_x\rangle$ (black), and $|m_f = +1, q = q_x - 2k_L\rangle$ (red), following unitary evolution under \hat{H}_{SOC} for times up to $100 \mu s$ at different spin-orbit coupling regimes: (i) $\Omega_0 = 9.9 E_L$, $\Omega = 0$, $\delta = 5.8 E_L$, (ii) $\Omega_0 = 0$, $\Omega = 8.6 E_L$, $\delta = -0.7 E_L$, $\delta\omega = \epsilon + 12 E_L$, and (iii) $\Omega_0 = 1.5 E_L$, $\Omega = 8.4 E_L$, $\delta = -4.7 E_L$, $\delta\omega = \epsilon + 17 E_L$. **b.** Occupation probability for long pulsing up to $800 \mu s$ for parameters as in (iii). **c.** Power spectral density of the occupation probability. We subtract the mean value of each probability before taking the Fourier transform to remove peaks at $f = 0$. The peaks in the PSD then correspond to the relative eigenenergies of \hat{H}_{SOC} .

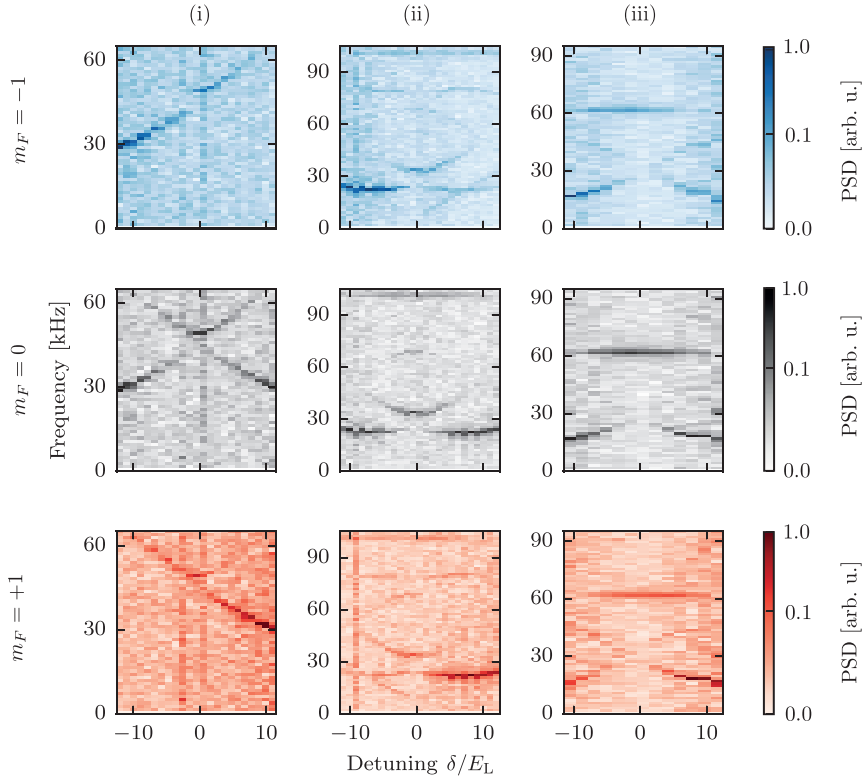


Figure 5.6: Power spectral density of the time dependent occupation probability for each state in the measurement basis for three coupling regimes: (Left) $\Omega_0 = 9.9E_L$, $\Omega = 0$, (Center) $\Omega_0 = 0$, $\Omega = 8.6E_L$, $\delta\omega = \epsilon + 12E_L$, and (Right) $\Omega_0 = 4.9E_L$, $\Omega = 8.4E_L$, $\delta\omega = \epsilon + 17E_L$. Each panel is normalized to peak amplitude to highlight small amplitude features in the PSD of the periodically driven SOC, and the highest value on the frequency axis corresponds to the FFT bandwidth.. **b.** Spin-dependent SOC dispersion for three different coupling regimes. We combine the PSD of the occupation probability of the states $|m_F = \pm 1, q_x = \mp 2k_L\rangle$, and shift each frequency by an amount proportional to the squared quasimomentum and the effective mass. The dashed lines are the calculated Floquet energies for the Hamiltonian using our calibration parameters.

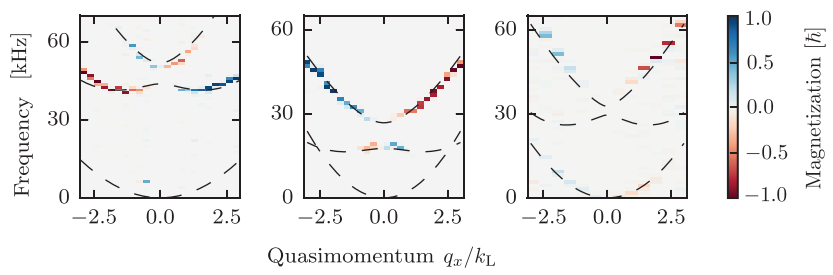


Figure 5.7: Spin-dependent SOC dispersion for three different coupling regimes. We combine the PSD of the occupation probability of the states $|m_F = \pm 1, q_x = \mp 2k_L\rangle$, and shift each frequency by an amount proportional to the squared quasimomentum and the effective mass. The dashed lines are the calculated Floquet energies for the Hamiltonian using our calibration parameters.

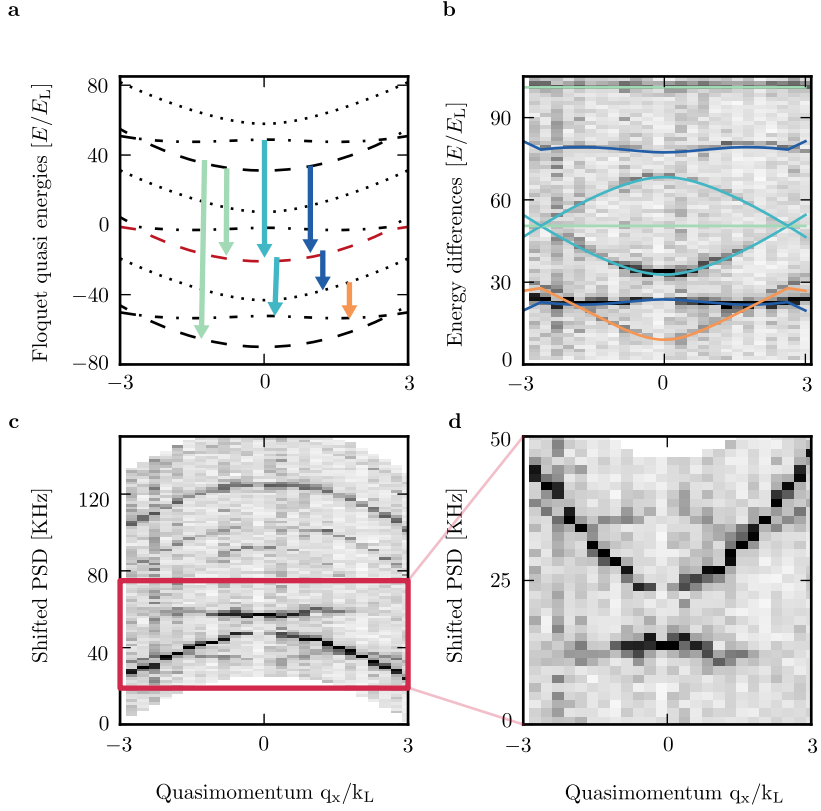


Figure 5.8: **a** Floquet quasi-energy spectrum of a SOC Hamiltonian with periodic coupling strength. The red line represents the eigenstate that has the largest overlap with the initial $|m_F = 0\rangle$ state. The arrows indicate the energies of the states that have non-zero overlap with the initial state and can be measured with Fourier transform spectroscopy. **b** PSD of the occupation probability and numerically calculated energy differences between the levels indicated by the arrows on panel a. **c** PSD shifted by a quadratic term $-\hbar^2 q_x^2 / 2m^*$. The red box indicates the region of interest where we can recover the SOC spectrum. **d** We invert the frequency axis and shift it by $\delta\omega$.

Chapter 6: Synthetic clock transitions through continuous dynamical decoupling

Most of the experiments and experimental techniques described so far have used the hyperfine $|m_F\rangle$ states as effective spins and dressed them with an RF or Raman field. However, due to the linear dependence of their energies with respect to magnetic field, and our lack of control of environmental changes we always had to take special care to stabilize the magnetic field on the lab (see Chapter 4.5.2). An alternative to doing active magnetic field stabilization is to use of ‘clock’ transitions which are first order insensitive to changes in magnetic field, however, they are not present in all systems or for arbitrary system parameters. However, under almost all circumstances, clock transitions can be synthesized using dynamical decoupling protocols. These protocols involve driving the system with an external oscillatory field, resulting in a dynamically protected ‘dressed’ system.

The idea of implementing continuous dynamical decoupling (CDD) in the lab came from a theoretical proposal to engineer Rashba type SOC using Raman beams and a strong RF field [19], the second being a necessary ingredient for CDD. We initially worked in implementing CDD protocols to create ‘synthetic clock states’ as an intermediate step towards our final goal of engineering Rashba SOC. Just like with Fourier spectroscopy, CDD became a workhorse of the lab both for the stability it provides against environmental fluctuations and because it has given us access to non-zero matrix coupling elements that we otherwise would not have when working with the bare $|m_F\rangle$ states. We have continued to use CDD not only for engineering Rashba SOC (Chapter 8) but also to engineer subwavelength optical lattices [12] and Hofstadter cylinders (work in preparation). On the theory side, we ~~also worked on~~ a proposal that uses them as a platform for emulating \mathcal{PT} symmetric Hamiltonians [20].

This Chapter discusses the implementation of CDD in our system of ultracold atoms. First I ~~will~~ give a general overview of dynamical decoupling and

continuous dynamical decoupling. Then I ~~will~~ describe the technical details and characterization of our CDD protocol which produces a protected three-level system of dressed-states and whose Hamiltonian is fully controllable. Finally I discuss an implementation of concatenated CDD that renders the system first-order insensitive to both magnetic field noise and noise in the control field. This work was published in [21] and was done in parallel with [22].

6.1 Basic principles of CDD

Dynamical decoupling (DD) protocols consist in applying an external control Hamiltonian, generally implemented by a series of pulses, which has the effect of canceling out the dynamics that arise from the quantum system coupling to the environment. DD was first introduced in the context of nuclear magnetic resonance (NMR) with the discovery of spin-echoes [23], where a ‘refocusing’ pulse was applied to eliminate dephasing of spins resulting from variations in magnetic field. These ideas were later generalized in [24] to protect a system from decoherence induced by interactions with a quantum environment. Continuous dynamical decoupling (CDD) relies on the application of time-periodic continuous control fields, rather than a series of pulses. Unlike conventional dynamical decoupling, CDD does not require any encoding overhead or quantum feedback measurements.

A number of dynamical decoupling protocols, pulsed or continuous, have been shown to isolate quantum systems from low-frequency environmental noise [25–33]. Thus far, CDD has inoculated multi-level systems in nitrogen vacancy centers in diamond, nuclear magnetic resonance experiments, and trapped atomic ions [34–41], from spatiotemporal magnetic field fluctuations.

6.2 CDD of a spin-1 system

We implemented CDD using a strong RF magnetic field with strength Ω , that linked the three $|m_F\rangle$ states comprising the $F = 1$ electronic ground state manifold of ^{87}Rb . The RF field was linearly polarized along \mathbf{e}_x , and had angular frequency ω close to the Larmor frequency $\omega_0 = g_F\mu_B B_0$ from a magnetic field $B_0\mathbf{e}_z$; g_F is the Lande g -factor and μ_B is the Bohr magneton. Using the rotating frame approximation for the frame rotating at ω (which

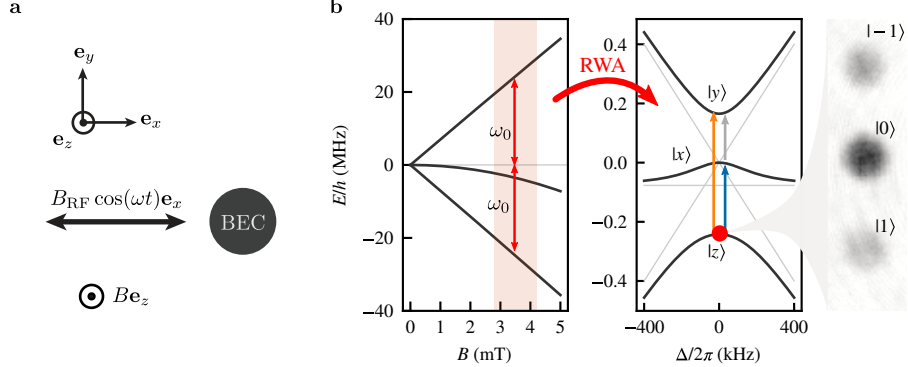


Figure 6.1: **a.** Setup for implementing CCD using a strong RF magnetic field. **b.** Left: dependence of the $5^2S_{1/2}$, $F = 1$ ground state of ^{87}Rb on magnetic field, where the quadratic dependence of the $|m_F = 0\rangle$ state's Zeeman shift has been exaggerated so it is visible on the same scale. Center: energies of the $|xyz\rangle$ eigenstates, for $\Omega/2\pi = 200$ kHz (black curves) and $\Omega = 0$ (grey curves). Right: TOF absorption image of $|z\rangle$ at $\Delta = 0$, showing the constituent $|m_F\rangle$ states.

is valid for $\omega \gg \Omega$), the system is described by

$$\hat{H} = \hbar\Delta\hat{F}_z + \hbar\epsilon(\hat{F}_z^2 - \hat{\mathbb{1}}) + \hbar\Omega\hat{F}_x, \quad (6.1)$$

with detuning $\Delta = \omega - \omega_0$; quadratic Zeeman shift ϵ ; spin-1 angular momentum operators $\hat{F}_{x,y,z}$; and identity operator $\hat{\mathbb{1}}$. For a detailed derivation of Equation 6.1 see Section 4.3.2.

6.3 The $|xyz\rangle$ states

The eigenstates of Equation 6.1 correspond to the CDD basis. In this section I describe their properties and show that they are first order insensitive to magnetic field fluctuations.

6.3.1 State decomposition

We denote the eigenstates of Equation 6.1 by $|x\rangle$, $|y\rangle$ and $|z\rangle$. They are linear combinations of the $|m_F\rangle$ basis states, and for $\Delta = 0$ the (non-

normalized) eigenvectors are:

$$\begin{aligned} |x\rangle &= |-1\rangle - |1\rangle, \\ |y\rangle &= |-1\rangle - \frac{\epsilon + \tilde{\Omega}}{\sqrt{2\Omega}} |0\rangle + |1\rangle, \\ |z\rangle &= |-1\rangle - \frac{\epsilon - \tilde{\Omega}}{\sqrt{2\Omega}} |0\rangle + |1\rangle. \end{aligned} \quad (6.2)$$

Figure 6.2 shows the full state decomposition as a function of Δ , where it can be seen that the $|xyz\rangle$ states adiabatically map to the $|m_F\rangle$ states for $\Delta \gg \Omega$: for positive (negative) detuning $|z\rangle$ maps to $|1\rangle$ ($|-1\rangle$); $|y\rangle$ maps in the exact opposite way to $|z\rangle$; and $|x\rangle$ always maps to $|0\rangle$.

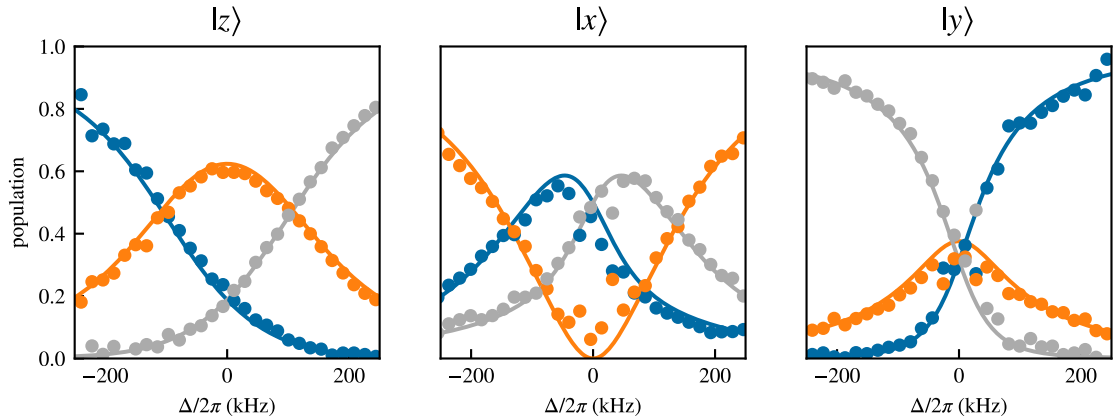


Figure 6.2: Decomposition of the $|xyz\rangle$ states on the $|m_F\rangle$ basis for $\Omega/2\pi = 145(1)$ kHz. The $|m_F = -1, 0, 1\rangle$ states correspond to blue, orange, gray respectively.

We labeled our dressed states $|xyz\rangle$ since for $\Omega \rightarrow 0^+$ and $\Delta = 0$, they con-

tinuously approach the $|XYZ\rangle$ states familiar from quantum chemistry [42]:

$$\begin{aligned} |X\rangle &= \frac{|1\rangle - |-1\rangle}{\sqrt{2}}, \\ |Y\rangle &= i \frac{|1\rangle + |-1\rangle}{\sqrt{2}}, \\ |Z\rangle &= |0\rangle. \end{aligned} \quad (6.3)$$

which transform under the application of the spin-1 operators as $\epsilon_{jkl}\hat{F}_j|k\rangle = i\hbar|l\rangle$, so that a resonant probe field can induce transitions between at least one pair of states, irrespectively of its polarization.

Finally, when $\Omega \rightarrow \infty$ they are independent of the driving field amplitude and continuously approach the eigenstates of the \hat{F}_x operator

$$\begin{aligned} |x\rangle &= |1\rangle - |-1\rangle, \\ |y\rangle &= |1\rangle + \sqrt{2}|0\rangle + |-1\rangle, \\ |z\rangle &= |1\rangle - \sqrt{2}|0\rangle + |-1\rangle. \end{aligned} \quad (6.4)$$

6.3.2 Energies

We can understand the clock-like nature of these states by looking at their eigenvalues which are even functions with respect to Δ as can be seen by the leading order expansion of the eigenenergies $E_i = \hbar\omega_i$ for $\Delta \rightarrow 0$

$$\begin{aligned} \omega_x &= -\frac{\epsilon}{\Omega^2}\Delta^2 + \mathcal{O}(\Delta^4), \\ \omega_y &= \frac{1}{2}(-\epsilon + \tilde{\Omega}) - \frac{(\epsilon + \tilde{\Omega})}{-\epsilon^2 - 4\Omega^2 + \epsilon\tilde{\Omega}}\Delta^2 + \mathcal{O}(\Delta^4), \\ \omega_z &= \frac{1}{2}(-\epsilon - \tilde{\Omega}) + \frac{(\epsilon - \tilde{\Omega})}{\epsilon^2 + 4\Omega^2 + \epsilon\tilde{\Omega}}\Delta^2 + \mathcal{O}(\Delta^4), \end{aligned} \quad (6.5)$$

where we have defined $\tilde{\Omega} = \sqrt{4\Omega^2 + \epsilon^2}$. The energy differences $\hbar\omega_{xy}$, $\hbar\omega_{zy}$ and $\hbar\omega_{zx}$ are only quadratically sensitive to Δ for $\Delta \ll \Omega$ ¹ so that detuning fluctuations $\delta\Delta$ are suppressed to first order, making these a trio of synthetic clock states. For the zx transition, the curvature of ω_x and ω_z has the same

¹The energies are quadratic in Δ for $\Delta \ll \Omega$, and linear for $\Delta \gg \Omega$ with a slope of 7 MHz/mT.

sign for $\epsilon < \tilde{\Omega}$ (Equation 6.5). Since the quadratic term changes curvature it can be made arbitrarily small. However, this cancellation does not take place when we consider the dependence of ϵ on Δ from the Breit-Rabi expression. However one can still find an optimal Ω for which ω_{zx} depends quartically on Δ .

6.3.3 Transition matrix elements

Unlike the $|m_F\rangle$ basis, an oscillatory magnetic field with the right polarization can drive transitions between all pairs of the $|xyz\rangle$ states with non-zero transition matrix elements. The transition matrix elements between the $|xyz\rangle$ have a dependence on both Ω and Δ . For the $\Delta = 0$ case they can be read from the representation of the spin-1 matrices in the $|xyz\rangle$ basis

$$\begin{aligned}\hat{F}_x &\rightarrow \begin{pmatrix} \frac{2\Omega}{\tilde{\Omega}} & 0 & -\frac{\epsilon}{\tilde{\Omega}} \\ 0 & 0 & 0 \\ -\frac{\epsilon}{\tilde{\Omega}} & 0 & -\frac{2\Omega}{\tilde{\Omega}} \end{pmatrix} \\ \hat{F}_y &\rightarrow \begin{pmatrix} 0 & -\frac{i(\tilde{\Omega}-\epsilon)}{\Omega\sqrt{\frac{(\epsilon-\tilde{\Omega})^2}{\Omega^2}+4}} & 0 \\ \frac{i(\tilde{\Omega}-\epsilon)}{\Omega\sqrt{\frac{(\epsilon-\tilde{\Omega})^2}{\Omega^2}+4}} & 0 & -\frac{i(\tilde{\Omega}+\epsilon)}{\Omega\sqrt{\frac{(\tilde{\Omega}+\epsilon)^2}{\Omega^2}+4}} \\ 0 & \frac{i(\tilde{\Omega}+\epsilon)}{\Omega\sqrt{\frac{(\tilde{\Omega}+\epsilon)^2}{\Omega^2}+4}} & 0 \end{pmatrix} \\ \hat{F}_z &\rightarrow \begin{pmatrix} 0 & -\frac{\sqrt{\frac{\epsilon}{\tilde{\Omega}}+1}}{\sqrt{2}} & 0 \\ -\frac{\sqrt{\frac{\epsilon}{\tilde{\Omega}}+1}}{\sqrt{2}} & 0 & -\frac{2}{\sqrt{\frac{(\tilde{\Omega}+\epsilon)^2}{\Omega^2}+4}} \\ 0 & -\frac{2}{\sqrt{\frac{(\tilde{\Omega}+\epsilon)^2}{\Omega^2}+4}} & 0 \end{pmatrix},\end{aligned}\quad (6.6)$$

where the states have been ordered by decreasing energy ($|y\rangle$, $|x\rangle$, $|z\rangle$). We can therefore see that a term in a Hamiltonian that is proportional to \hat{F}_x can only drive transitions between $|z\rangle$ and $|y\rangle$ and that coupling terms proportional to \hat{F}_y and \hat{F}_z can drive both drive transitions between $|z\rangle$ and $|x\rangle$ or $|x\rangle$ and $|y\rangle$ with different strengths. It can be seen from Equation 6.6 that

when Ω and ϵ are comparable in magnitude there exists at least one non-zero transition matrix element for each pair of dressed states and they can all be coupled cyclically.

6.4 $|xyz\rangle$ state preparation

We implemented CCD to BECs with $N \approx 5 \times 10^4$ atoms. For all of the experiments described in this Chapter the dipole trap had trapping frequencies of $(f_x, f_y, f_z) = (42(3), 34(2), 133(3))$ Hz. We applied a $B_0 \approx 3.27$ mT bias field that lifted the ground state degeneracy, giving an $\omega_0/2\pi = 22.9$ MHz Larmor frequency, with a quadratic shift $\epsilon/2\pi = 76.4$ kHz. We determined that the ambient magnetic field fluctuations were dominated by contributions from line noise giving an rms uncertainty $\delta\Delta/2\pi = g_F\mu_B\delta B/h = 0.67(3)$ kHz.

The state preparation consisted of two stages of ARP. On the first stage we followed the usual protocol described in Chapter 4.4.2 to prepare the BEC in any of the $|m_F = 0, -1, 1\rangle$ states. On the second stage we adiabatically transformed the $|m_F\rangle$ states into the $|xyz\rangle$ states. We started with the bias field far from resonance ($\Delta(t=0)/2\pi \approx -450$ kHz) and with all coupling fields off. Then we ramped on Ω in a two-step process. We first ramped from $\Omega = 0$ to an intermediate value Ω_{mid} , approximately half its final value in 1 ms. We then ramped Δ to zero in 3 ms by increasing the magnetic field B_0 . After allowing B_0 to stabilize for 30 ms, we ramped the RF dressing field to its final value Ω in 1 ms, yielding the dynamically decoupled $|xyz\rangle$ states. It was important that the wait for the field to stabilize was performed at an intermediate Ω_{mid} as we found several times that the capacitors on the impedance matching network of the antenna used to generate the RF field would burn if we kept the power on for too long. After performing any experiment with the $|xyz\rangle$ states we measured their populations by adiabatically deloading them back into the $|m_F\rangle$ basis. We first ramped B_0 so that Δ approached its initial detuned value in 2 ms, and then ramped off the dressing RF field in 1 ms. A typical experimental sequence for Δ and Ω can be visualized in Figure 6.4. As usual, we obtained the spin-resolved momentum distribution using absorption imaging after TOF, with a Stern-Gerlach field to spatially separate the spin components. The right panel of Figure 6.1b shows a TOF image of the $|m_F\rangle$ state decomposition of the $|z\rangle$ state. For this image as well as for the measurement of the dressed state decomposition shown in Figure 6.2 we suddenly (not-adiabatically) turned the RF coupling

off, thereby projecting the $|xyz\rangle$ states back into the $|m_F\rangle$ basis.

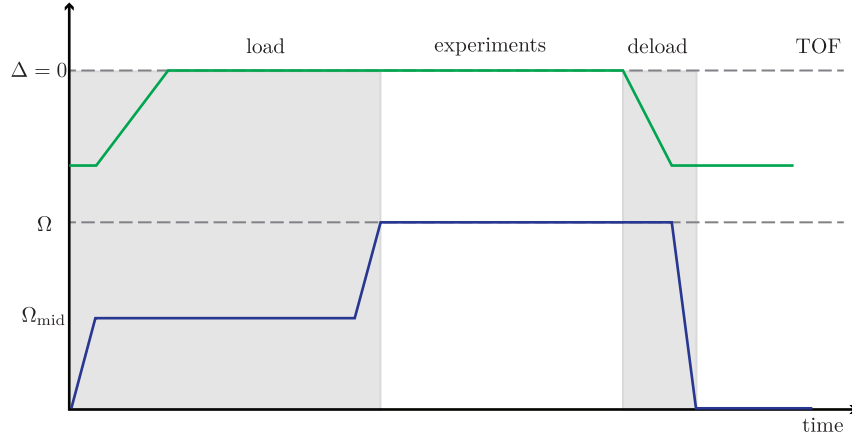


Figure 6.3: Detuning and RF coupling strengths ramps (not to scale) performed to adiabatically prepare the $|xyz\rangle$ states starting in the $|m_F\rangle$ states and vice versa.

6.5 Initial characterization of Ω

Producing RF fields with large coupling strength was not a trivial task and when testing different antenna designs it was important to have an easy and quick way of characterizing them. We mostly relied on two different techniques to get an initial estimate of Ω : first, we prepared atoms in $|m_F = -1\rangle$ and pulse on the RF to drive transitions between the three $|m_F\rangle$ states. We would then fit the populations in the three states as a function of pulsing time to the time evolution given by propagating the time dependent Schrödinger equation using the RF Hamiltonian (Equation 6.1) with Ω and Δ as free parameters.

Alternatively, we followed the loading procedure described in Section 6.4 but suddenly turned Ω off for different values of Δ to get the decomposition of the $|xyz\rangle$ states in terms of $|m_F\rangle$ states. We then fit the populations to the eigenstates of the Equation 6.1 with Ω and Δ as free parameters. Figure 6.2 is an example of such type of calibration.

For an antenna with a high quality factor such as ours ($q \sim 20$) we could not ‘suddenly’ turn Ω on or off as it takes some time for power to build

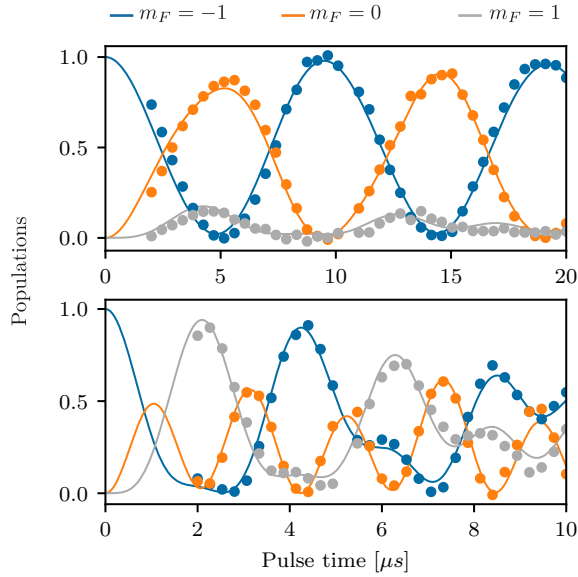


Figure 6.4: We prepared the system in the $|m_F = 0\rangle$ state and pulsed Ω and fit the populations in the $|m_F\rangle$ states as a function of pulsing time to get an initial estimate of Ω . The top panel shows the time evolution of $\Omega/2\pi \approx 76$ kHz and the bottom panel shows the evolution for $\Omega/2\pi \approx 238$ kHz

up and to die out when the RF fields are turned on or off. If we did not include this into the model used to calibrate Ω we could get some results that were slightly off. In the end we only used this measurements as initial estimates and once we found an antenna design that could produce a large enough Ω we used the spectroscopy techniques described in next section to fully characterize the system.

6.6 Spectroscopy

We confirmed our control and measurement techniques spectroscopically by measuring the energy differences between the $|xyz\rangle$ states with an additional probing field with angular frequency $\omega + \omega_p$, coupling strength Ω_p and polarized along \mathbf{e}_y . In the frame rotating with angular frequency ω and after

using a RWA the system was described by the Hamiltonian

$$\begin{aligned}\hat{H} = & \Delta\hat{F}_z + \hbar\epsilon(\hat{F}_z^2/\hbar^2 - \hat{\mathbb{I}}) + \Omega\hat{F}_x \\ & + \Omega_p(\sin(\omega_p t)\hat{F}_x + \cos(\omega_p t)\hat{F}_y).\end{aligned}\quad (6.7)$$

In this rotating frame the probe field initially polarized along \mathbf{e}_y has components along \mathbf{e}_x and \mathbf{e}_y , resulting in at least one non-zero transition matrix element for all transitions between pairs of dressed states. If the probing field was polarized along \mathbf{e}_z we would not be able to drive the zy transition as can be seen from the matrix elements in Equation 6.6.

To probe the dependence on detuning of the $|xyz\rangle$ state energies, we pulsed Ω_p on for a constant time and scanned ω_p for different values of Δ . Figure 6.1b shows the spectroscopically resolved values of $\omega_{xy}/2\pi$, $\omega_{yz}/2\pi$, and $\omega_{zx}/2\pi$ for $\Omega/2\pi = 194.5(1)$ kHz and the side panel shows a sample spectra measured with coupling strength $\Omega_p/2\pi \approx 1$ kHz and $\Delta/2\pi \approx 9$ kHz. The dashed curves were computed by diagonalizing Equation 6.1, and they clearly depart from our measurements for the zx transition. This departure results from neglecting the weak dependence of the quadratic shift ϵ on bias field B_0 . In near-perfect agreement with experiment, the solid curves from the full Breit-Rabi expression account for this dependency.

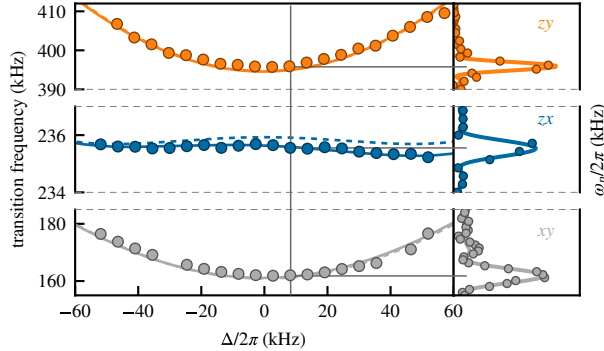


Figure 6.5: Left: spectroscopic data showing transitions between the $|xyz\rangle$ states for $\Omega/2\pi = 194.5(1)$ kHz. The vertical scale of the center panel (zx transition) has only 10% the range of the other panels. The dashed lines correspond to the Hamiltonian of Equation 6.1 while the solid lines include the dependence of the quadratic shift on Δ . Right: representative spectra.

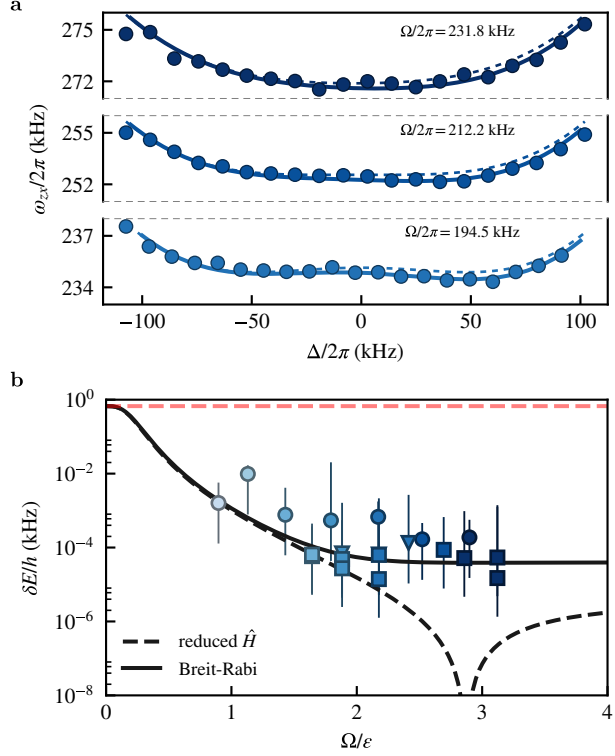


Figure 6.6: **a.** Transition frequency $\omega_{zx}/2\pi$ for three values of $\Omega/2\pi$. The dashed curves correspond to Equation 6.7, while the solid curves use the Breit-Rabi expression. **b.** The change in energy from our experimental detuning fluctuations as measured in the $|m_F\rangle$ basis is $\delta\Delta/2\pi = 0.67$ kHz (red dashed line). Triangles correspond to $|xyz\rangle$ spectroscopy data, squares to side-of-peak π -pulse data, and circles to double-dressed data. The black dashed (solid) curve was calculated using Equation 6.7 (the Breit-Rabi expression). The shading of the data points corresponds to the Rabi frequencies in Figure 6.8.

6.7 Robustness

To characterize the robustness of the $|xyz\rangle$ states, we focus on the zx transition which can be made virtually independent of magnetic field variations due to the similar curvature of $\omega_z(\Delta)$ and $\omega_x(\Delta)$ (see the middle panel of Figure 6.1b). We quantified the sensitivity of this transition to field

variations with three methods corresponding to the different markers in Figure 6.6b: (1) Triangles denote data using full spectroscopic measurements similar to Figure 6.6a. (2) Squares denote data in which a detuned π -pulse of the probe field transferred approximately half of the atoms from $|z\rangle$ to $|x\rangle$. This ‘side-of-peak’ technique overcomes the limitation of Rabi spectroscopy being first-order insensitive to changes in ω_{zx} . (3) Circles describe data using a double dressing technique that will be described in Section 6.9. In each case we measured the energy shift from resonance as a function of detuning (magnetic field) and then used a fourth order polynomial fit to extract the rms residuals $\delta\omega_{zx}$ due to the known detuning noise². The results are not consistent with the theory simple from Equation 6.7 (dashed) and instead require the Breit-Rabi expression (solid) to obtain full agreement³.

Even at our smallest coupling $\Omega/2\pi = 69(1)$ kHz the typical magnetic field noise was attenuated by two orders of magnitude, rendering it essentially undetectable. Ideally, the radius of curvature of $\omega_{zx}(\Delta)$ changes sign at about $\Omega/2\pi = 220$ kHz, leaving only a Δ^4 contribution, however, in practice the small dependence of ϵ on B prevents this perfect cancellation.

6.7.1 Optimal response to noise

The sensitivity of the zx transition to detuning fluctuations can be optimized further by working at $\Delta \neq 0$ as shown in Figure 6.7. This behavior can only be captured by including the dependence of the quadratic shift on Δ as given by the Breit-Rabi expression.

For small values of Ω the optimum value of Δ corresponds to one of the concave features of the zx transition energy that arise due to the asymmetry introduced by the quadratic shift. As Ω gets larger, these features merge into a single one and the optimum value is $\Delta \approx 0$. The deviation from $\Delta = 0$ is due to an overall tilt of the transition energy coming from the dependence of the quadratic shift on Δ . At the optimum point $\Omega/\epsilon \approx 3$ the sensitivity of the synthetic clock transition is 1.9×10^{-7} kHz, c.f., the ^{87}Rb clock transition which scales as 57.5 kHz/mT² and gives 5.8×10^{-7} kHz.

²Our procedure also quantifies the small fluctuations that survive for spectra that are flat beyond second order, as in Equation 6.1.

³The fluctuations can be even smaller for a given Ω if we allow for $\Delta \neq 0$.

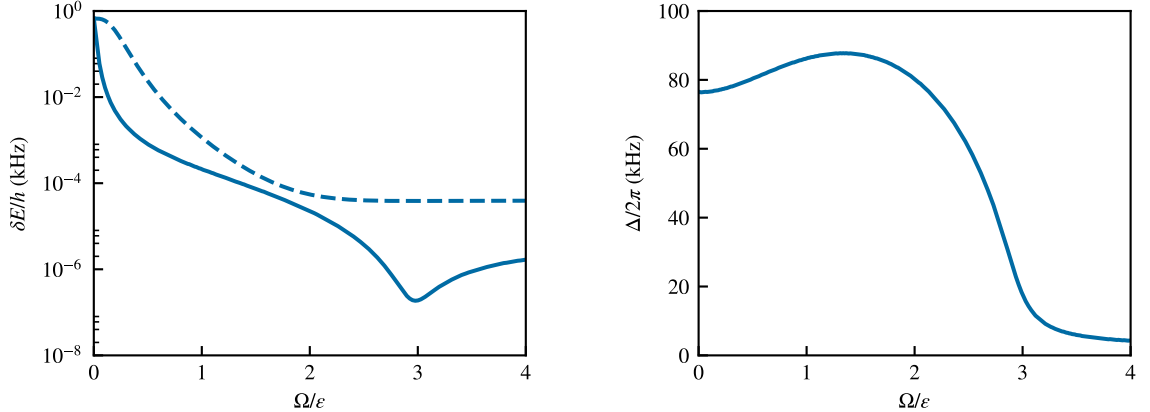


Figure 6.7: Left: The optimum response (solid) of the zx transition to detuning fluctuations allowing for finite Δ compared to $\Delta = 0$ (dashed) for the full Breit-Rabi model. Right: The values of Δ that correspond to the minimum derivative of ω_{zx} .

6.8 Driving dressed state transitions

We explored the strength of the probe-driven transitions between these states by observing coherent Rabi oscillations (Figure 6.8a) where our BEC was prepared in $|z\rangle$ and the probe field had strength $\Omega_p/2\pi \approx 1$ kHz. The top panel shows Rabi oscillations between $|m_F = 0\rangle$ and $|m_F = -1\rangle$ states for reference, and the remaining panels show oscillations between $|z\rangle$ and $|x\rangle$. The observed Rabi frequency between dressed states decreased with increasing Ω indicating a dependence of the zx transition matrix elements on Ω . We repeated this experiment driving all possible pairs of dressed state transitions at fixed Ω_p for, and Figure 6.8b shows the dependence of these matrix elements on Ω for $\Delta = 0$.

The coherence of the Rabi oscillations for longer times was limited by gradients in Ω that lead to phase separation of the dressed states, and therefore loss of contrast in the oscillations. This effect was faster for smaller frequency Rabi oscillations. For example for $\Omega_p/2\pi = 5$ kHz we observed coherent Rabi oscillations with almost full contrast for more than 10 ms while for the $\Omega_p/2\pi = 870$ Hz oscillation shown in Figure 6.9 the contrast was significantly reduced after 5 ms. The loss of contrast was even worse when we

tried performing a Ramsey sequence where the time evolution is most sensitive to the environment. One solution to this problem would be to change the experimental setup to a double loop antenna to generate a more spatially uniform magnetic field.

In comparison, we found that for both Rabi and Ramsey oscillations between the $|m_F\rangle$ states the phase started deteriorating after a few hundreds of μs , this is not surprising due to bias magnetic field temporal noise. We cancelled gradient magnetic fields so that no phase separation of the bare states was observed for $> 10 \text{ sec}$. As a result, the system can in principle undergo coherent evolution without loss of contrast for a long time but because of field fluctuations between shots what we actually observe is full contrast noise.

6.9 Concatenated CDD

The driving field Ω coupled together the $|m_F\rangle$ states, giving us the $|xyz\rangle$ synthetic clock states that were nearly insensitive to magnetic field fluctuations. However, the spectrum of these states is first-order sensitive to fluctuations $\delta\Omega$ of the driving field. Reference [29] showed that an additional field coupling together with these $|xyz\rangle$ states can produce doubly-dressed states that are insensitive to both $\delta\Omega$ and $\delta\Delta$: a process called concatenated CDD. In our experiment, the probe field provided the concatenating coupling field. Because $\Omega_p \ll \Omega$, we focus on a near-resonant two-level system formed by a single pair of dressed states, here $|z\rangle$ and $|x\rangle$, which we consider as pseudospins $|\uparrow\rangle$ and $|\downarrow\rangle$. These are described by the effective two-level Hamiltonian

$$\hat{H}_p = \frac{\hbar\Delta'}{2}\hat{\sigma}_3 + \hbar\Omega' \cos(\omega_p t)\hat{\sigma}_1, \quad (6.8)$$

with energy gap $\Delta' \approx \omega_{z,x}$ (shifted by off-resonant coupling to the zy and xy transitions) and coupling strength $\Omega' \propto \Omega_p$, as set by the matrix elements displayed in Figure 6.8b. Here $\hat{\sigma}_{1,2,3}$ are the three Pauli operators.

We perform a second transformation into a frame rotating with angular frequency ω_p and use a RWA to compute the eigenenergies of Equation 6.8. For large values of Ω' the energies take the values $E_{\uparrow,\downarrow} \approx \pm\Omega'/2 + (\Delta')^2/2\Omega'$. Even though $E_{\uparrow,\downarrow}$ are still first order sensitive to Ω because $\Delta' \approx \omega_{z,x} \propto \Omega$, its effect is suppressed by a factor of $1/\Omega'$. Thus, the concatenated CDD field protects from the fluctuations $\delta\Delta'$ of the first dressing field in a similar way

that CDD provided protection from detuning noise $\delta\Delta$. Table 6.1 summarize⁴ the dependence of the $|xyz\rangle$ and $|\uparrow\downarrow\rangle$ energies on Δ , Ω and Ω' .

Table 6.1: Energies of the CDD and CCDD states as a function of Δ , Ω and Ω' . The dependence on parameters not relevant to the expansion is given by the functions f_1 , f_2 , g_1 and g_2 .

	CDD	concatenated CDD
Δ dependence	$f_1(\epsilon, \Omega)\Delta^2$	$f_2(\Omega, \epsilon)\frac{\Delta^2}{\Omega'}$
Ω, Ω' dependence	$\Omega + g_1(\Delta, \epsilon)\frac{1}{\Omega}$	$\left[\Omega^2 + \epsilon\Omega + g_2(\Delta, \epsilon)\frac{1}{\Omega}\right]\frac{1}{\Omega'}$

We produced doubly-dressed states by doing (one more!) ARP sequence. We initialized the system in the $|\Downarrow\rangle$ state with RF coupling strength Ω_i . We set the probe frequency to be ~ 20 kHz off resonant with respect to the $|\downarrow\rangle \rightarrow |\uparrow\rangle$ transition and ramped it on in 10 ms. We then ramped $\Omega_i \rightarrow \Omega_f$ in 30 ms. The experimental sequence can be visualized in Figure 6.10. We chose the value of Ω_f such that it would bring ω_p to resonance at $\Delta = 0$, creating double dressed states that were equal superposition of $|\downarrow\rangle$ and $|\uparrow\rangle$. We quantified the sensitivity of this transition to large changes in the detuning Δ in terms of the fractional population imbalance $\langle\hat{\sigma}_3\rangle = P_\downarrow(\Delta) - P_\uparrow(\Delta)$, shown in Figure 6.11a for $\Omega_f/2\pi = 138.2(1)$ kHz⁴. This signal is first-order sensitive to $\omega_{\downarrow,\uparrow}$, and provided our third measurement of sensitivity to detuning in Figure 6.6b denoted by circles.

We compared the fidelity of preparing a superposition of the $|\downarrow\rangle$ and $|\uparrow\rangle$ states to adiabatically preparing a similar superposition of the the $|m_F = 0\rangle$ and $|m_F = -1\rangle$ states using a single ARP (no dressed states involved), both with a probe field strength of ≈ 1 kHz. Figure 6.11b shows the rms deviation of the population imbalance measured over a few hundred repetitions of the

⁴We chose the maximum value of Δ such that the population of $|y\rangle$, was negligible after deloading.

experiment. The rms deviation for the dressed basis is 0.024(1) and is an order of magnitude smaller than for the $|m_F\rangle$ basis 0.29(1), where it is practically impossible to prepare a balanced superposition for the parameters used here⁵.

Figure 6.11c shows the response of the $|\downarrow\rangle \rightarrow |\uparrow\rangle$ transition to small changes $\delta\Omega$ for different values of Ω_p . We prepared an equal superposition of $|\downarrow\rangle$ and $|\uparrow\rangle$ following the same procedure as before for $\Omega_f/2\pi = 138.2(1)$ kHz. We then measured how the population imbalance changes for small variations of Ω — the effective detuning in the ‘twice-rotated frame’ — for different probe amplitudes Ω_p . We defined a sensitivity parameter $d\langle\hat{\sigma}_3\rangle/d\Omega$, obtained from the linear regime of the population imbalance measurements (see inset in Figure 6.11c). The robustness of the doubly-dressed states against $\delta\Omega$ fluctuations increased with Ω_p , thus verifying the concatenating effect of CDD in the $|xyz\rangle$ basis.

However promising the application of multiple concatenating fields might seem, this procedure has a fundamental limitation. Each time a new coupling field is applied the energies of the dressed states are reduced to something on the order of magnitude of the applied concatenating field. For example, in the experiments we have described here we started with $|m_F\rangle$ with transition frequencies on the order of MHz. The transition frequencies of the $|xyz\rangle$ states are reduced to hundreds of kHz (or in general the magnitude of Ω). After applying the second concatenating RF field the transition frequencies of the $|\uparrow\rangle$ are of the order of Ω_p which needs to be smaller than Ω in order for the second RWA to be valid. Therefore we see that after applying multiple concatenating fields we are at the risk of having some very robust states that are also very closely spaced in energy which might not be desirable for some applications.

6.10 Conclusions

We realized a three-level system that is dynamically decoupled from low-frequency noise in magnetic fields, measured now-allowed transitions between all three states, and demonstrated control techniques for creating arbitrary Hamiltonians. These techniques add no heating or loss mechanisms, yet within the protected subspace retain the full complement of cold-atom co-

⁵In Figure 6.11b, the noise in the $|m_F\rangle$ basis is not Gaussian distributed as is typical of line noise in these experiments.

herent control tools such as optical lattices and Raman laser coupling, and permit new first-order transitions that are absent in the unprotected subspace. These transitions enable experiments requiring a fully connected geometry as for engineering exotic states, e.g., in cold-atom topological insulators, and two-dimensional Rashba spin-orbit coupling in ultracold atomic systems [19, 43].

The synthetic clock states form a decoherence-free subspace that can be used in quantum information tasks where conventional clock states might be absent, or incompatible with other technical requirements [44]. Moreover, their energy differences are proportional to the amplitude of the dressing field, and hence tunable, so they can be brought to resonance with a separate quantum system. The effective quantization axis can be arbitrarily rotated so that the two systems can be strongly coupled, pointing to applications in hybrid quantum systems [45, 46]. Introducing a second coupling field shields the system from fluctuations of the first, a process which can be concatenated as needed. More broadly, synthetic clock states should prove generally useful in any situation where fluctuations of the coupling field can be made smaller than those of the environment.

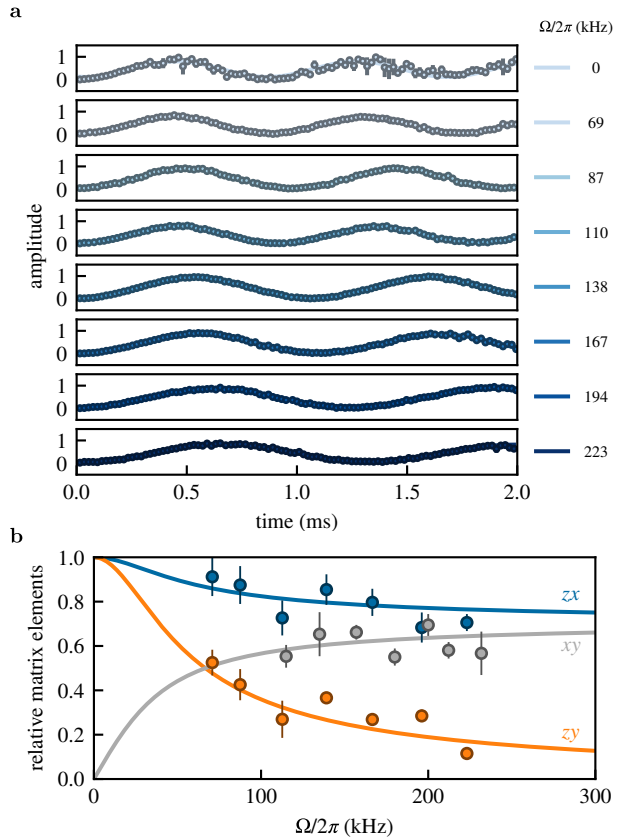


Figure 6.8: **a.** Rabi oscillations. Phase coherence is maintained throughout the oscillations in the dressed basis, while it is quickly lost in the $|m_F\rangle$ basis. The marker size reflects the typical uncertainties on the dressed basis oscillations. **b.** Transition matrix elements for zx (blue) and zy (orange) transitions decrease monotonically with increasing Ω for $\Delta = 0$, while they increase for xy .

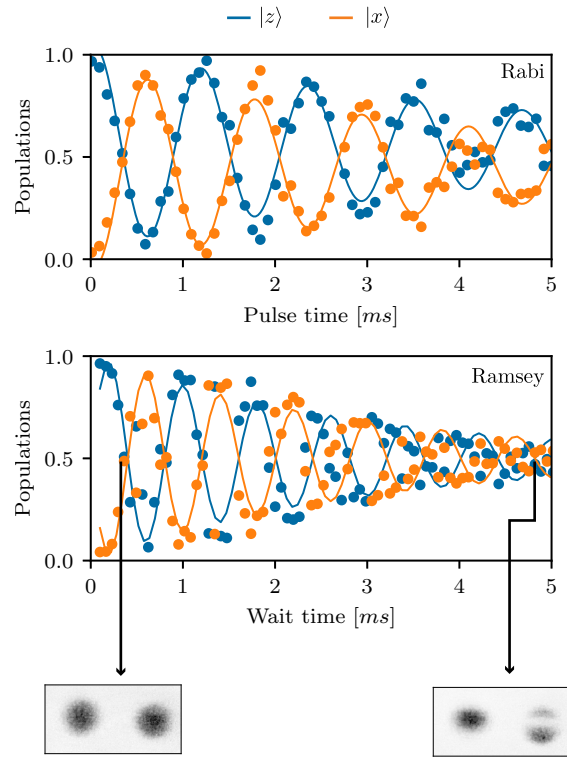


Figure 6.9: Loss of contrast in coherent oscillations. A Rabi oscillation (top) between the $|z\rangle$ and $|x\rangle$ states with $\Omega_p/2\pi = 870$ Hz decays by $1/e$ in 4.6 ms and a Ramsey oscillation (middle) with about 1 kHz frequency decays in about 3 ms. The gradients in Ω lead to phase separation of dressed states and loss of contrast for longer pulse/wait times.

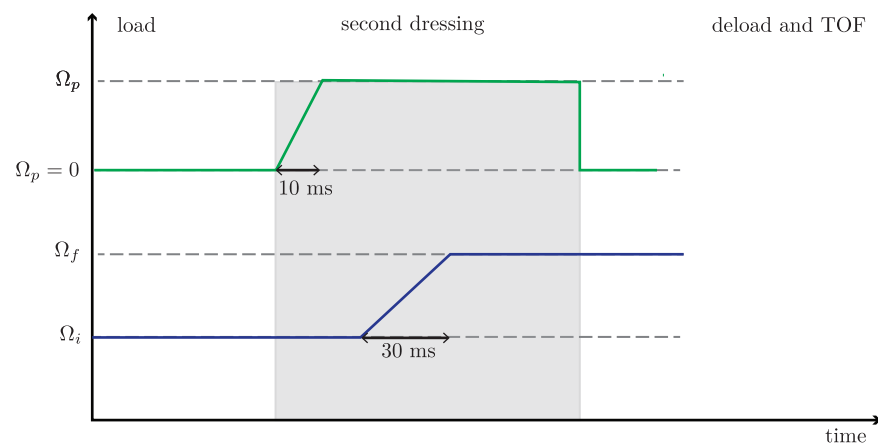


Figure 6.10: Experimental protocol for implementing concatenated CDD. We started an initial RF coupling strength Ω_i and ramped on the probe field Ω_p in a few ms with $\omega_p = \omega_{z,x}(\Omega_f)$ so that it was initially slightly off resonant with the zx transition. We then ramped the the RF field to Ω_f , brining ω_p to resonance.

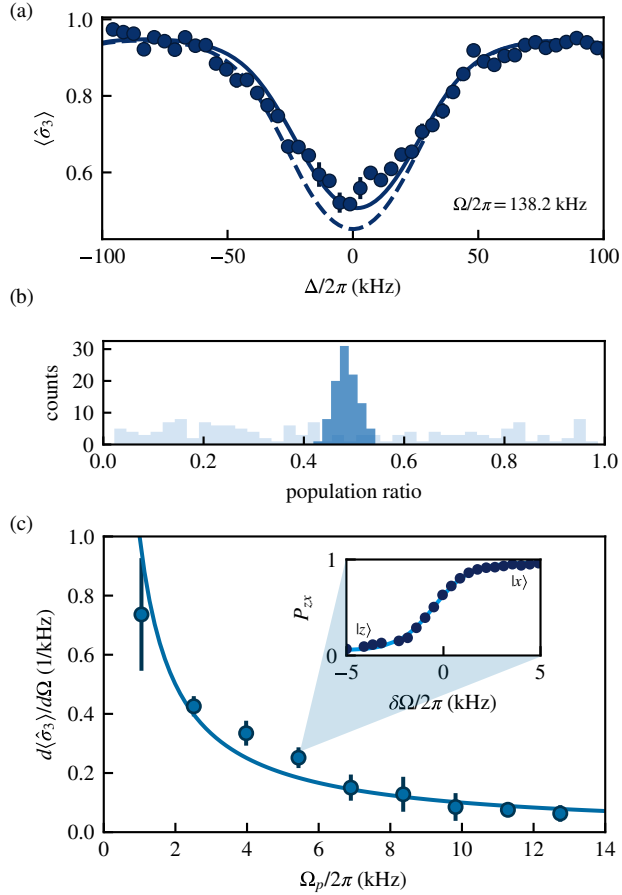


Figure 6.11: (a) The fractional population imbalance of the $\downarrow\uparrow$ transition for $\Omega/2\pi = 138.2(1)$ kHz over detuning Δ . The dashed curve is calculated using Equation 6.7 and the solid one using the full Breit-Rabi expression. (b) The fidelity of preparing a balanced superposition of $|\downarrow\rangle$ and $|\uparrow\rangle$ (dark blue) states compared to $|m_F = 0\rangle$ and $|m_F = -1\rangle$ states (light blue). (c) The robustness of \downarrow, \uparrow transition against fluctuations $\delta\Omega$ for different probe field coupling strengths. The points represent the slope of the fitted curves to the fractional population imbalance (inset).

Chapter 7: Topological order in quantum systems

Topological order can be found in a wide range of physical systems, from crystalline solids [47], photonic meta-materials [48] and even atmospheric waves [49] to optomechanic [50], acoustic [51] and atomic systems [52]. Topological systems are a robust foundation for creating quantized channels for transporting electrical current, light, and atmospheric disturbances. These topological effects can be quantified in terms of integer-valued invariants such as the Chern number, applicable to the quantum Hall effect [53, 54], or the \mathbb{Z}_2 invariant suitable for topological insulators [55].

We got interested in topology when working on engineering Rashba [56] type spin-orbit coupling in the lab. Our system had non-trivial topology but it broke from the usual mold of topological materials as it didn't have an underlying crystalline structure that conventionally yields to integer Chern numbers.

Before describing our experiments that characterize the unconventional topology of a Rashba spin-orbit coupled gas, in this Chapter I take a step back to describe the basic concepts of topology and its applications to the band theory of solids. The ideas of topology and how exactly one can connect donuts with band structures might feel a bit obscure and complicated for non-experts in the field. I wrote this Chapter with that in mind, with the hope that it can be followed by non-experts and provide some insight and intuition about this field. The concepts introduced in this Chapter will be necessary for understanding the results presented in Chapter 8.

7.1 Topology in mathematics

Topology is a branch of mathematics that studies continuity [57]. The most familiar example might be that of objects being continuously deformed into one another. For example, a donut can be continuously deformed into a coffee mug but if we want to deform it into a pretzel we need to poke more

holes in it. This gives us some intuition that the donut and the mug must share the same topology, which is different from that of the pretzel. Topology also studies more abstract objects but I will limit the discussion to closed two-dimensional surfaces  in three dimensions, which will be enough to provide some intuition when we define topological invariants for band structures in the following sections.

The topology of 2D surfaces can be classified by the Euler characteristic, and it is related to the local Gaussian curvature of a surface by the Gauss-Bonet theorem. The Gaussian curvature can be interpreted in the following way: at any point in a surface we can find a normal vector which is orthogonal to the tangent plane of the surface. We can then define a family of planes containing the normal vector and their intersection with the surface defines a family of curves. The curvature of any of these curves at the point where the planes intersect, which is equal to the quadratic coefficient in a Taylor expansion around that point, is called the normal curvature κ . When we consider all the normal curvatures, the minimum and maximum of these are called the principal curvatures and are used to define the Gaussian curvature at any point of a surface $K = \kappa_{min}\kappa_{max}$ [57]

The Gauss-Bonnet theorem states that the integral of the local Gaussian curvature over the whole surface is equal to the integer valued Euler characteristic

$$\chi = \frac{1}{2\pi} \int_S K dA, \quad (7.1)$$

which is related to the genus g (number of holes or handles in the surface) by $\chi = 2(1 - g)$. The Gauss-Bonnet theorem is a very powerful result as it relates the local properties of a surface, the Gaussian curvature, with a global topological invariant, the Euler characteristic.  [Add picture to describe principal curvatures?]

In the following sections I will introduce topological invariants in the context of condensed matter physics, which even though might seem a bit more abstract, their interpretation can be closely related to the concepts just defined in this section.

7.2 Topological order in condensed matter

Just like topology classifies properties of geometric objects, one important task of condensed matter physics has been to classify phases of matter. Many

of these phases, for example magnetic or conducting phases, can be described in terms of order parameters related to spontaneously broken symmetries [58]. However, in the past few decades and increasing number of systems have been found where it is only possible to understand their phases and properties in terms of the underlying topology of their quantum states. This new paradigm of physics has been so important that in 2016 the Nobel prize in physics was awarded to David J. Thouless, F. Duncan M. Haldane and J. Michael Kosterlitz for the theoretical discoveries of topological phase transitions and topological phases of matter

The effects of topology in condensed matter systems were first observed when von Klitzing and colleagues [59] measured the quantized Hall resistance in two-dimensional electron gases subjected to a strong perpendicular magnetic field. The effect can be understood semi-classically by thinking of the electrons' quantized cyclotron orbits¹ that give rise to Landau levels. If the Landau levels are filled then there is an energy gap separating two consecutive levels and the material acts as an insulator but if an electric field is applied the orbits drift and the electrons will be 'skipping orbits' in the edge as can be seen in Figure 7.1, giving rise to what is known as edge states.

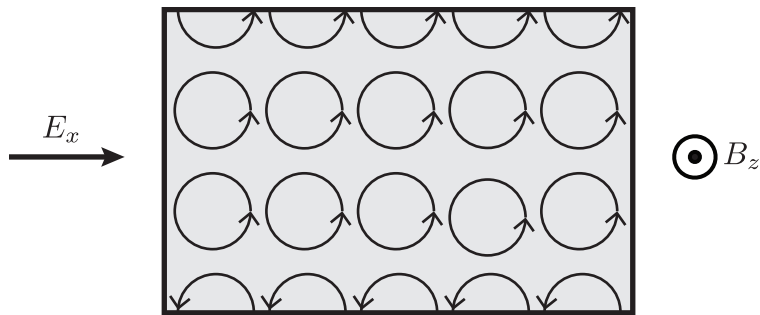


Figure 7.1: The quantum Hall effect. An electron gas is confined in a two-dimensional material and a strong magnetic field is applied perpendicular to the plane. The electrons on the bulk travel in cyclotron orbits while the electrons on the edge travel 'skipping orbits'.

¹This is an intuitive but not very complete explanation of the quantum Hall effect, see [60] if you want to learn more about this subject.

In a seminal paper Thouless, Kohomoto, Nightingale, and den Nijs [53] explained that the quantization of the Hall conductivity is determined by the underlying topology of the band structure. Just like the Euler characteristic defined in Equation 7.1 classifies 2D solids that can be continuously deformed without opening or closing holes, there is a topological invariant that classifies band structures that can be deformed into one another without opening or closing an energy gap. This invariant, initially known as the ‘TKNN invariant’, was later recognized by the mathematical physicist Barry Simon as the ‘first Chern class invariant from $U(1)$ fiber bundles’ [61]² and the TKNN invariant became what is known today as the Chern number or Chern invariant. Another very valuable contribution from Simon’s work was that he made the connection between the Chern number and the Berry’s geometrical phase [63] which will be defined in the following sections and will allow us to make a physical interpretation of this otherwise abstract seeming topological invariant.

7.3 Berry phase and Berry curvature

A Berry or geometric phase is used to describe the phase acquired by a quantum state as it moves through a closed trajectory in parameter space. It plays a key role in topological band theory and can help provide a physical interpretation of the Chern number.

Consider a Hamiltonian \hat{H} that depends on a set of parameters $\mathbf{r} = (r_1, r_2, \dots)$. If the parameters are slowly changed in time, the corresponding change in the system can be described by a path in parameter space $\mathbf{r}(t)$. The state $|\psi(t)\rangle$ evolves according to the time dependent Schrödinger equation and at any given time t there is a basis that satisfies

$$\hat{H}(\mathbf{r}) |n(\mathbf{r})\rangle = E_n(\mathbf{r}) |n(\mathbf{r})\rangle \quad (7.2)$$

for $\mathbf{r} = \mathbf{r}(t)$. Suppose the system is initially in state $|n(\mathbf{r}(t=0))\rangle$, if the parameters are changed slowly such that the adiabatic theorem is valid, then at time t the state of the system can be written as

$$|\psi(t)\rangle = \exp \left\{ -\frac{i}{\hbar} \int_0^t dt' E_n(\mathbf{r}(t')) \right\} \exp(i\gamma_n(t)) |n(\mathbf{r}(t))\rangle, \quad (7.3)$$

²See [62] if you want to dive into hardcore topology.

where the first exponential term corresponds to a dynamical phase factor, and the second term is a geometric phase. By imposing that $|\psi(t)\rangle$ satisfies the time-dependent Schrödinger equation one finds that

$$\gamma_n(t) = i\langle n(\mathbf{r}) | \nabla_{\mathbf{r}} n(\mathbf{r}) \rangle \cdot \dot{\mathbf{r}}(t), \quad (7.4)$$

where the term

$$\mathbf{A}_n(\mathbf{r}) = i\langle n(\mathbf{r}) | \nabla_{\mathbf{r}} n(\mathbf{r}) \rangle \quad (7.5)$$

is usually referred to as the Berry connection³ or the Berry vector potential for reasons that will become apparent. Because eigenvectors can only be defined up to a global phase, \mathbf{A} is a gauge dependent quantity. If we make a gauge transformation such that $|n(\mathbf{k})\rangle \rightarrow e^{i\xi(\mathbf{k})} |n(\mathbf{k})\rangle$ then the Berry connection is also transformed as $\mathbf{A}_n(\mathbf{k}) \rightarrow \mathbf{A}_n(\mathbf{k}) - \nabla_{\mathbf{k}}\xi(\mathbf{k})$. However if we integrate the Berry connection on a closed loop

$$\gamma_n(\mathcal{C}) = \oint_{\mathcal{C}} \mathbf{A}_n(\mathbf{r}) \cdot d\mathbf{l}, \quad (7.6)$$

we obtain the Berry phase which, unlike the Berry connection, is gauge independent (modulo 2π).

An alternative way to compute Berry's phase uses Stokes's theorem from vector calculus

$$\begin{aligned} \oint_{\mathcal{C}} \mathbf{A}_n \cdot d\mathbf{l} &= \int_S \nabla \times \mathbf{A}_n \cdot d\mathbf{S} \\ &= \int_S \boldsymbol{\Omega}_n \cdot d\mathbf{S}, \end{aligned} \quad (7.7)$$

where the vector field $\boldsymbol{\Omega}_n = \nabla \times \mathbf{A}_n$ is known as the Berry curvature or Berry fieldT. By rewriting the Berry phase in this way, its resemblance with the definition of the Euler characteristic from Equation 7.1 becomes apparent.

Using some vector calculus identities the Berry curvature can be rewritten as

³This is related to the connection defined in differential geometry that is used to describe things like parallel transport.

$$\begin{aligned}
\boldsymbol{\Omega}_n &= i[\nabla_{\mathbf{r}} \langle n |] \times [\nabla_{\mathbf{r}} |n \rangle] \\
&= \sum_{j \neq n} i[\langle n | \nabla_{\mathbf{r}} |j \rangle] \times [\langle j | \nabla_{\mathbf{r}} |n \rangle] \\
&= i \sum_{j \neq n} \frac{\langle n | \nabla_{\mathbf{r}} \hat{H} |j \rangle \times \langle j | \nabla_{\mathbf{r}} \hat{H} |n \rangle}{(E_j - E_n)^2},
\end{aligned} \tag{7.8}$$

where $\langle n | \nabla_{\mathbf{r}} |j \rangle$ was replaced with $\langle n | \nabla_{\mathbf{r}} \hat{H} |j \rangle / (E_j - E_n)$ by differentiating Equation 7.2. This expression shows that $\boldsymbol{\Omega}_n$ is a gauge independent quantity as it does not depend on the derivatives of a particular gauge choice for $|n\rangle$ but rather on $\nabla_{\mathbf{r}} \hat{H}$ which is gauge independent. Also we can see that $\boldsymbol{\Omega}_n$ becomes singular when there are degeneracies present in the Hamiltonian, and these degeneracies act as ‘sources’ for the Berry connection. Finally, even though the system may remain in state $|n\rangle$ during the adiabatic evolution, this expression for the Berry curvature makes it explicit that other eigenstates of the Hamiltonian have an influence in the Berry phase acquired.

7.3.1 Aharonov-Bohm phase as an example of a Berry’s phase

A familiar example of geometric phases is the Aharonov-Bohm phase [64] gained by electrons moving along closed trajectories around a solenoid. This phase was initially conceived as a way of showing that in quantum mechanics magnetic vector potentials, typically conceived only as mathematical objects, can have a physical effect on the wave function. They considered a coherent electron beam split into two paths around a solenoid that produces a magnetic field \mathbf{B} as shown in Figure 7.2. Outside the solenoid the magnetic field $\mathbf{B} = 0$, but there can be a non-zero magnetic vector potential such that $\mathbf{B} = \nabla \times \mathbf{A}$. The two beams are later recombined. Even though the electron’s trajectories are not modified, when looking at the interference pattern one finds that the two paths acquired different phases, and their difference is remarkably equal to magnetic flux piercing the area enclosed by the electrons path $\Delta\varphi = 2\pi\Phi_B/\Phi_0$, where $\Phi_0 = h/e$ is the flux quantum.

This Aharonov-Bohm phase can be interpreted as an example of a Berry phase in real space. For a charged particle in the presence of a vector potential the momentum dependence of the free-particle Hamiltonian is modified $\mathbf{p} \rightarrow \mathbf{p} - q\mathbf{A}$ so that the wave function will depend on the magnetic vector

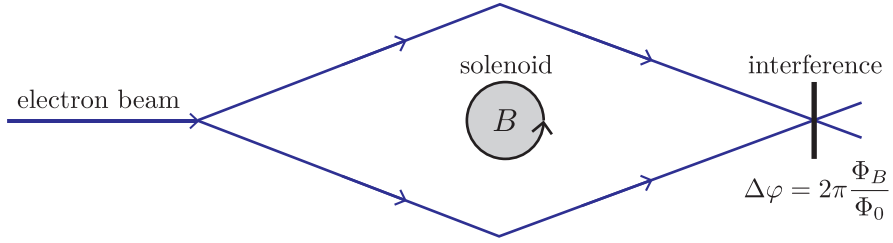


Figure 7.2: The Aharonov-Bohm experiment. A coherent electron beam is split into two paths surrounding a solenoid which produces a non-zero magnetic field \mathbf{B} inside the gray region and $\mathbf{B} = 0$ outside. The two beams are later recombined and an interference pattern reveals a phase difference $\Delta\varphi = 2\pi\Phi_B/\Phi_0$ equal to the magnetic flux enclosed by the electron's path.

potential as well. Using Equations 7.6 and 7.7 it can be shown that the Berry phase associated to a closed path around the solenoid is exactly equal to the Aharonov-Bohm phase:

$$\begin{aligned}\gamma_n(\mathcal{C}) &= \frac{e}{\hbar} \oint_{\mathcal{C}} \mathbf{A}(\mathbf{r}) \cdot d\mathbf{r} \\ &= \frac{e}{\hbar} \int_S \nabla \times \mathbf{A} \cdot d\mathbf{S} \\ &= \frac{e\Phi_B}{\hbar},\end{aligned}\tag{7.9}$$

For this particular example, the Berry connection is exactly equal to the magnetic vector potential and the Berry curvature is the magnetic field. This gives us a very physical intuition for interpreting the Berry phase in terms of the ‘magnetic flux’ from abstract sources of ‘magnetic fields’ in parameter space.

7.3.2 Chern number

The Chern number is conventionally used to describe the topology of materials which have an underlying crystalline structure. According to Bloch’s theorem, the wave functions of a space periodic Hamiltonian can be written as $|\psi(\mathbf{k})\rangle = e^{i\mathbf{k}\cdot\mathbf{r}} |u(\mathbf{k})\rangle$, where $|u(\mathbf{k})\rangle$ are periodic wave functions. If we



define the Bloch Hamiltonian

$$\hat{H}(\mathbf{k}) = e^{i\mathbf{k}\cdot\mathbf{r}} \hat{H}(\mathbf{r}) e^{-i\mathbf{k}\cdot\mathbf{r}}, \quad (7.10)$$

their eigenvectors are given by $|u(\mathbf{k})\rangle$ and the eigenvalues define the band structure. Translational symmetry implies that $\hat{H}(\mathbf{k} + \mathbf{a}) = \hat{H}(\mathbf{k})$ where \mathbf{a} is a reciprocal lattice vector. The crystal momentum or quasimomentum is only defined within the periodic Brillouin zone and therefore can be mapped into a torus in d dimensions if we glue the edges together.

The Chern number of the n th band is defined as

$$C_n = \frac{1}{2\pi} \int_{BZ} \Omega_n d\mathbf{k}, \quad (7.11)$$

where the relevant parameter space is crystal momentum and the surface of integration corresponds to the BZ (a torus). The definition of Chern number is closely related to the definition of the Berry phase from Equation 7.7. For our previous example of a quantum Hall system, the integer proportionality factor in the quantized conductance is exactly equal to the Chern number.

Just like two-dimensional surfaces are classified by the integral of their Gaussian curvature, the topology of Bloch bands and of quantum systems in general is determined by the integral of the Berry curvature. In a similar way, the integral connects local properties of a quantum system, the Berry connection, with a global topological invariant, the Chern number. One subtle difference is that the Euler characteristic is only determined by the surface (and its intrinsic Gaussian curvature) while the Chern number is defined both by a surface (the BZ) and an additional local curvature (the Berry curvature). By studying different Hamiltonians one can obtain a different Berry curvature, but the geometry of the BZ and thereby the surface of integration is typically defined by a torus⁴. This difference will be important later on when we describe the experiments performed to study a system with Rashba spin-orbit coupling and an unconventional topology.

7.4 The bulk-edge correspondence principle

Earlier I mentioned that topological systems provide very robust channels for transporting things like electrical current and light. This transport

⁴In next chapter we consider a case where this breaks down.

phenomena typically arises when there is a spatial interface between two topologically distinct phases. The electrons skipping orbits at the interface of a (topological) quantum Hall material and (trivial) vacuum are one example of this. Notice that for this particular example the modes propagate along a given direction, they are chiral. In general one can expect to have modes moving along two directions, and the difference between the number of these modes $N_L - N_R$ is fixed and determined by the topology of the bulk states. The bulk-edge correspondence principle relates the difference in the number of these modes with the bulk topology of the materials at the interface:

$$\Delta C = N_R - N_L \quad (7.12)$$

where ΔC is the difference of Chern number on the interface.

7.5 Example: two-level model

Many of the concepts introduced in the previous section can be readily applied and understood using a two-level model

$$\hat{H}(\mathbf{k}) = \mathbf{h}(\mathbf{k}) \cdot \hat{\boldsymbol{\sigma}} \quad (7.13)$$

where $\hat{\boldsymbol{\sigma}} = (\sigma_x, \sigma_y, \sigma_z)$ are the Pauli matrices and $\mathbf{h}(\mathbf{k}) = (h_x(\mathbf{k}), h_y(\mathbf{k}), h_z(\mathbf{k}))$ are functions of \mathbf{k} . This model has been used to describe a number of physical systems like graphene [54] and spin-orbit coupled systems [56, 65]. Let us now consider the simple case $h(\mathbf{k}) = \mathbf{k}$, for which $\nabla_{\mathbf{k}} \hat{H} = \boldsymbol{\sigma}$ and using Equation 7.8 it can be shown that

$$\Omega = -\frac{\mathbf{h}}{2h^3} \quad (7.14)$$

which can be recognized as the field of a Dirac monopole [66] with charge $-1/2$. The degeneracy in the energies that gives rise to the monopole is known as a Dirac point as the energies in that vicinity resemble the dispersion of a massless Dirac particle. It follows from Equation 7.14 that the Berry phase gained by moving in a closed path \mathcal{C} is equal to the flux from the monopole in the surface enclosed by \mathcal{C} as is shown in Figure 7.3. This connects nicely with our intuition from the Aharonov-Bohm effect. For a closed surface enclosing the Dirac point, the Chern number is an integer equal to 1.

For a Hamiltonian with arbitrary $\mathbf{h}(\mathbf{k})$ we can define a normalized vector

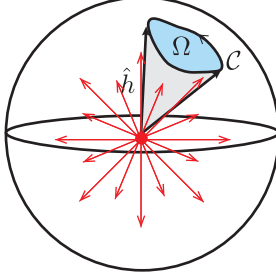


Figure 7.3: For a two-level system, the Berry curvature from a Dirac point can be viewed as a Dirac monopole in momentum (parameter) space. The Chern number can be interpreted as the flux from the monopole on the solid angle subtended by the vector $\hat{h}(\mathbf{k})$ or alternatively as the number of times $\hat{h}(\mathbf{k})$ wraps around a unit sphere.

$\hat{h} = \mathbf{h}/|\mathbf{h}|$ and the Chern number takes the form

$$C = \frac{1}{4\pi} \int (\partial_{k_x} \hat{h} \times \partial_{k_y} \hat{h}) \cdot \hat{h} d\mathbf{k} \quad (7.15)$$

and can be interpreted as the number of times that the vector $\hat{h}(\mathbf{k})$ wraps around a unit sphere [67], a quantity that is known as the winding number.

7.6 Monopoles and Dirac strings

We just gained some intuition about interpreting the Chern number as the flux from Dirac monopoles. But if we stick to our knowledge of electromagnetism we might remember that monopoles are forbidden since

$$\int_S \mathbf{B} \cdot d\mathbf{S} = \int_V (\nabla \cdot \mathbf{B}) dV \quad (7.16)$$

and $\nabla \cdot \mathbf{B} = \nabla \cdot (\nabla \times \mathbf{A}) = 0$. how is this possible? The solution to this problem was envisioned by Dirac [66] and is now called a Dirac string. If we consider an semi-infinitely long and infinitesimally thin solenoid, the magnetic field in the finite end will resemble that of a monopole as can be

seen in Figure 7.4. This tiny solenoid corresponds to the Dirac string. A

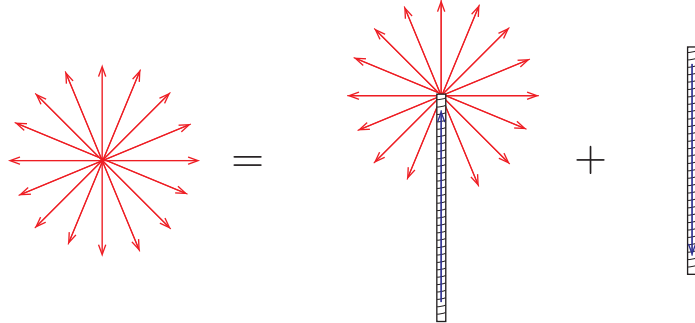


Figure 7.4: For a two-level system, the Berry curvature from a Dirac point can be viewed as a Dirac monopole in momentum (parameter) space. The Chern number can be interpreted as the flux from the monopole on the solid angle subtended by the vector $\hat{h}(\mathbf{k})$ or alternatively as the number of times $\hat{h}(\mathbf{k})$ wraps around a unit sphere.

more mathematical interpretation of these strings comes from the fact that the vector potential of a monopole has ‘lines’ where it becomes singular. For example for a particular gauge we can write

$$\mathbf{A}(\mathbf{r}) = g \frac{-y\mathbf{e}_x + x\mathbf{e}_y}{r(r+z)} \quad (7.17)$$

which is singular for the negative z axis where $z = -r$. The orientation of the Dirac string is gauge dependent, something that should not surprise or bother us at this point. However, the physical effects of the Dirac string should be gauge independent, or in other words, the Aharonov-Bohm phase gained by a charged particle moving in a path that encloses the string should be an integer multiple of 2π . This argument gives rise to the Dirac charge quantization [66], and in the context of topology, it guarantees that when we calculate the Berry phase by integrating the Berry connection (vector field) along a path that encloses a Dirac string, its effect will be indistinguishable.

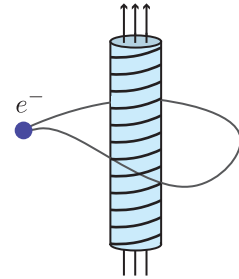
7.7 Conclusions

Topology plays a very important role both in math and in physics. In this Chapter I reviewed the basic concepts of topology in the context of condensed matter physics that will be relevant for our experiments with unconventional topology. As a closing remark, Figure 7.5 summarizes the main concepts that were introduced and is a reminder that topological invariants are global properties defined in terms of integrals of local properties. Furthermore, we can use our intuition from electromagnetic theory to interpret topological invariants in quantum mechanics.

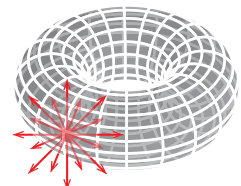
Euler characteristic



Magnetic flux



Chern number



$$\chi = \frac{1}{2\pi} \int_{\mathcal{M}} K dS$$

$$n = \frac{2e}{h} \int_{\mathcal{M}} \mathbf{B} \cdot d\mathbf{S}$$

$$C = \frac{1}{2\pi} \int_{\mathcal{M}} \boldsymbol{\Omega} \cdot d\mathbf{S}$$

Figure 7.5: The Euler characteristic and the Chern number are topological invariants defined by integrals of local curvatures. The Aharonov-Bohm phase gives us physical intuition to interpret the Chern number as the flux from a ‘Berry field’.